Compressible Turbulent Boundary Layer Simulations: Resolution Effects and Turbulence Modeling

Jonathan Poggie*

Air Force Research Laboratory, Wright-Patterson AFB, Ohio 45433-7512 USA

Direct numerical simulation (DNS) and high-fidelity, implicit large-eddy simulation (HFILES) were carried out for turbulent boundary layers at Mach 2.3 and 4.9. Transition to turbulence was promoted with an artificial body force trip. Two main projects were carried out in this work. First, the effects of spatial resolution on spectra and other flow statistics were examined for the baseline Mach 2.3 turbulent boundary layer flow. The finest grid in the spatial resolution study consisted of 3.3×10^{10} points, and maintained $\max(\Delta x_1^+, \Delta x_2^+, \Delta x_3^+) \leq 1$ everywhere. Examining velocity spectra in detail, HFILES was seen to converge seamlessly to DNS as the spatial resolution was increased. Further, turbulence statistics were found to be essentially independent of the domain width for values between two and eight times the maximum boundary layer thickness. Second, variations from the baseline flow conditions were considered, and the results compared to an algebraic model for the turbulent energy flux developed by R. Bowersox (J. Fluid Mech., vol. 633, pp. 61–70, 2009). An impressive match was obtained between the model and simulations, for a wide range of wall temperature and Mach number.

I. Introduction

This project aims to explore turbulent boundary layer flow in the context of direct numerical simulation (DNS), high-fidelity, implicit large-eddy simulation (HFILES), and Reynolds-averaged Navier-Stokes simulation (RANS). In particular, the present work focuses on assessing how well models at these different levels of approximation serve as tools for predicting the properties of turbulent boundary layer flow, and, given large-scale computing resources, whether high-resolution methods can be used in design.

Here DNS designates an approach where all significant turbulence length scales are resolved in the simulation. Implicit large-eddy simulation (ILES) is a general approach[1] in which the additional dissipation needed to account for the unresolved scales is provided directly by the numerical scheme. The terminology HFILES is intended to be more specific than ILES; the HFILES approach[2] uses high-order spatial differencing with filtering, and numerical dissipation is added only at the smallest spatial scales. In RANS, all turbulent fluctuations are modeled, and only the mean flow is computed. Intermediate levels of modeling, employing subgrid-scale models, are not considered here.

A. Turbulent Boundary Layer Physics

The structure of turbulence in compressible boundary layer flow cannot be considered well-understood, because neither experiments nor simulations can currently resolve the full range of space and time scales for conditions relevant for high-speed flight.[3–6] Thus, much of the understanding of turbulence in this regime comes from extrapolation of ideas developed for low-Reynolds-number, incompressible flow.

In the low-speed regime, coherent structures are believed to be the primary mechanism for the transport of mass, momentum, and energy across the boundary layer,[3] and for the entrainment of irrotational freestream fluid into the vortical boundary layer flow.[7,8] The inner part of the boundary layer ($y^+ < 100$) is characterized by alternating streaks of high and low speed fluid.[9] These streaks are persistent in space and time, and tend to be spaced about $\Delta z^+ \approx 100$ apart in the spanwise direction. The streaks have been observed to lift up

*Senior Aerospace Engineer, AFRL/RQHF. Associate Fellow AIAA.

from the wall, oscillate, and break up between $y^+ = 10$ and $y^+ = 30$. This inner layer burst cycle is believed to be the dominant mechanism for turbulence energy production in the boundary layer.[10]

Bulges are the dominant structure in the outer part of the boundary layer, from the beginning of the wake region to beyond the mean boundary layer edge ($y/\delta \approx 1.2$). The bulges are on the order of the boundary layer thickness in scale, and freestream fluid tends to penetrate close to the wall between the bulges. Studies of outer layer structure have found that a strong shear layer exists on the upstream side of these bulges, formed when high-speed freestream fluid impacts onto slow-moving fluid within the bulges.[11]

In supersonic flow, the large-scale structures have been studied using hotwires,[12–15] particle image velocimetry,[16] wall pressure transducers,[17] and flow visualization.[18,19] The primary effect of compressibility on turbulent boundary layers is the conversion of mechanical energy to heat through compression and viscous dissipation.[4,5] Near the wall, these factors cause the temperature to increase and the density to drop. The Reynolds number near the wall tends to decrease rapidly with increasing Mach number, a change that may have a strong effect on the turbulence structure in that region.[4,5,20]

If the fluctuating Mach number is small, Morkovin[21] proposed that the turbulence structure is similar to that of the incompressible case, with the primary difference being the property variation across the boundary layer. The principal support for this hypothesis is that a coordinate transform accounting for the fluid property variation succeeds in collapsing profiles of both mean velocity and turbulence statistics onto corresponding incompressible flow profiles.[4–6,22,23] When the fluctuating Mach number is larger, the turbulence structure could be significantly modified by compressible flow phenomena like eddy shocklets and sound radiation. Such effects have been documented for turbulent free shear layers.[24]

B. Compressible Turbulent Boundary Layer Simulations

A number of previous high-fidelity simulations (DNS and ILES) of compressible, wall-bounded flows[25–46] have been reported in the literature. Early simulations include studies by Coleman et al.[25,26] of channel flow. These studies focused on plane channels at Mach 1.5 and 3.0. Despite very strong property variations across the channel, the van Driest transformation[22] was found to collapse the data very well onto incompressible channel flow results. Direct compressibility effects were found to be very small.

The first direct numerical simulation of a supersonic turbulent boundary layer was carried out by Rai et al.[27] for a freestream Mach number of 2.25. The flow was spatially evolving, and tripped using a blowing and suction method. Again, scaling with local density was found to collapse the computational results onto incompressible flow data. Similar results were obtained later by Guarini et al.,[28] who carried out simulations of a turbulent boundary layer at Mach 2.5 using a mathematical model that assumed slow boundary layer growth in the streamwise direction.

Maeder et al.[29] expanded the Mach number range significantly, using a temporal approach to study boundary layers at Mach 3, 4.5, and 6. The results were generally consistent with local density scaling despite the higher Mach number range. Nonetheless, some deviation from the predictions of Morkovin's hypothesis was observed for the detailed turbulence statistics.

Urbin and Knight[30] adapted the rescaling-recycling technique[47] to supersonic flow to carry out simulations of turbulent boundary layer at Mach 3. Comparing an implicit large-eddy simulation approach to the Smagorinsky subgrid-scale model, they obtained nearly identical results with the two approaches. Rescaling and recycling were also used by Stolz and Adams[31] and Sagaut et al.,[34] who considered turbulent boundary layers at Mach 2.5 and 2.3, respectively.

With a spatially evolving approach, Rizzetta and Visbal[33] compared implicit large-eddy simulations to simulations with subgrid-scale models for a Mach 2.3 boundary layer, and again found little difference between the predictions of the different approaches.

Pirozzoli et al.[32] carried out simulations of a spatially evolving turbulent boundary layer at Mach 2.25. The boundary layer was tripped to turbulent flow using unsteady blowing and suction. The study again confirmed that direct compressibility effects are negligible for this Mach number range, and that a modified strong Reynolds analogy holds.

Pirozzoli's group has gone on to study Mach 2.0 boundary layers in detail.[37,44,46] Excellent comparison to incompressible flow DNS was obtained using Morkovin's scaling. They computed two-point correlations for large-scale structure shape, and the resulting structure angle compared well to the hotwire data of Spina.[48] They also compared spanwise and streamwise auto-correlation to experiment, and examined velocity-temperature correlation and turbulent Prandtl number. In their highest Reynolds number simulations,[46] in which $\delta^+ \approx 4000$, they observed a full decade of log-law in the mean velocity, a variation of peak

$\rho\overline{u'^2}/\tau_w$ with $\log\delta^+$, a clear $k^{-5/3}$ inertial subrange in spectra, and a k^{-1} range in the near-wall spectra. The group has also investigated wall pressure fluctuations.[40,45]

The research group of M. P. Martín has examined the effects of inflow conditions,[35,36] wall temperature,[39] Mach number,[41] and high enthalpy.[42] Further, Ringuette et al.[38] investigated coherent structures at Mach 3, and observed the long streamwise structures reported in the experiments of Ganapathisubramani et al.[49]

Lagha et al.[43] studied supersonic, turbulent boundary layer flows over a very large Mach number range (2.5–20), assuming ideal gas flow and employing the rescaling-recycling technique to generate the inflow. Real gas effects were not included because the main point of the study was to assess the effect of compressibility independent of these effects. Even over this large Mach number range, they found that the main turbulence statistics, when scaled by local density, were similar to the analogous incompressible statistics. The turbulent Mach number did not exceed 0.5 as the freestream Mach number was varied from 5 to 20.

Resolution and conditions reported for these various simulations of supersonic turbulent boundary layers are given in Table 1. Typical resolution recommendations[50,51] for wall-resolving large-eddy simulation are $50 \le \Delta x_1^+ \le 150$, $(\Delta x_2^+)_w < 1$, $15 \le \Delta x_3^+ \le 40$, and $\Delta t^+ < 1$. (The conventional inner variable scaling is used here: $\Delta t^+ = u_\tau^2 \Delta t/\nu_w$ and $(\Delta x_2^+)_w = u_\tau(\Delta x_2)_w/\nu_w$, where $u_\tau = \sqrt{\tau_w/\rho_w}$ is the friction velocity.) Corresponding recommendations for direct numerical simulation tighten the streamwise and spanwise resolution to the range $10 \le \Delta x_1^+ \le 20$ and $5 \le \Delta x_3^+ \le 10$. A wide range of spatial resolutions, spanning the range of LES and DNS, were reported for the studies listed in Table 1: $\Delta x_1^+ = 1.3$–59, $(\Delta x_2^+)_w = 0.1$–3.6, $\Delta x_3^+ = 1.2$–29. The grid resolution at the boundary layer edge $(\Delta x_2^+)_e$ has not been well documented. The reported domain width, relative to the maximum boundary layer thickness, has ranged over $L_3/\delta = 0.84$ to 3.8.

Because of the cost of such simulations, only limited spatial resolution studies have been carried out in these investigations of compressible turbulent boundary layer flows. Published resolution recommendations are a best estimate based on the available data. With the exception of the temporal simulation of Maeder et al.[29] at Mach 6 on a very small domain ($2.3\delta_0 \times 3.0\delta_0 \times 1.4\delta_0$), no study appears to have approached direct numerical simulation in the strictest sense, where the maximum mesh spacing in inner scaling is $\Delta\ell^+ \approx 1$.

To address this deficiency, the present study examined in detail the effects of spatial resolution on spectra and other flow statistics for a supersonic turbulent boundary layer flow at Mach 2.3 and $\delta^+ \approx 600$. The finest grid in the spatial resolution study consisted of 3.3×10^{10} points, and maintained $\max(\Delta x_1^+, \Delta x_2^+, \Delta x_3^+) \le 1$ everywhere on a domain with $L_3/\delta = 2.0$. Further, the effect of varying domain width between 2 and 8 local boundary layer thicknesses was examined. With this done, an additional project was carried out, comparing the results of simulations under different conditions to the algebraic energy flux model of Bowersox.[52,53]

II. Procedure

Supersonic turbulent boundary layer flows were explored using direct numerical simulation and high-fidelity, implicit large-eddy simulation. The numerical scheme was based on sixth-order compact spatial differences, second-order implicit time advancement, and eighth-order filtering. Rectangular grids with smooth stretching were employed, and transition from laminar to turbulent flow was promoted through a trip based on an artificial body force.

A. Physical Model

The calculations were carried out using the code HOPS (Higher Order Plasma Solver), developed by the author.[54–68] The code includes several physical models and numerical schemes. Here, the physical model consists of the perfect-gas, compressible-flow Navier-Stokes equations. The conservation of mass, momentum, and energy are expressed as:

$$\frac{\partial \rho}{\partial t} + \frac{\partial}{\partial x_j}(\rho u_j) = 0 \tag{1}$$

$$\frac{\partial}{\partial t}(\rho u_i) + \frac{\partial}{\partial x_j}(\rho u_j u_i - \Sigma_{ji}) = f_i \tag{2}$$

$$\frac{\partial \mathcal{E}}{\partial t} + \frac{\partial}{\partial x_j}(u_j \mathcal{E} - \Sigma_{ji} u_i + Q_j) = f_i u_i + S \tag{3}$$

where ρ is the gas density, u_i is its velocity, Σ_{ij} is the total stress tensor, $\mathcal{E} = \rho(\epsilon + u_i u_i/2)$ is the total fluid energy, ϵ is the internal energy, and Q_i is the heat flux. An optional body force f_i and energy source term S are included on the right hand side of the equations.

The total stress tensor Σ_{ij} is given by the usual constitutive equation for a Newtonian fluid, and the heat flux Q_i follows Fourier's heat conduction law:

$$\Sigma_{ij} = -p\delta_{ij} + \mu\left(\frac{\partial u_i}{\partial x_j} + \frac{\partial u_j}{\partial x_i}\right) - \frac{2}{3}\mu\frac{\partial u_k}{\partial x_k}\delta_{ij} \tag{4}$$

$$Q_i = -k\frac{\partial T}{\partial x_i} \tag{5}$$

where p is the pressure, μ is the viscosity, and k is the thermal conductivity. The transport coefficients were evaluated using the correlations given by White.[69] The working fluid (air) was assumed to be a calorically and thermally perfect gas: $\epsilon = c_v T$ and $p = \rho R T$, where T is the temperature, c_v is the specific heat, and R is the ideal gas constant.

B. Numerical Methods

The numerical approach was based on compact spatial differencing, filtering, and an implicit time-marching scheme. Employed in this manner as a perfect-gas, compressible-flow Navier-Stokes solver, the HOPS code is similar to the AFRL code FDL3DI.[70,71] A previous publication[67] showed good comparison between the HOPS and FDL3DI codes in a large-eddy simulation of a supersonic turbulent boundary layer flow. (See Pirozzoli[44] for alternative approaches, and for a general review of numerical methods for high-speed flows.)

The conservation laws were solved using an approximately-factored, implicit scheme, related to those developed by Beam and Warming[72] and Pulliam.[73] All calculations were carried out using double-precision arithmetic. Applying the standard transformation from physical coordinates x_i to grid coordinates ξ_i, the conservation equations (1)–(3) can be written in the form:

$$\frac{\partial \overline{U}}{\partial t} + \frac{\partial \overline{E}_j}{\partial \xi_j} = \frac{\partial \overline{E}_j^v}{\partial \xi_j} + \overline{S} \tag{6}$$

where the usual notation[74] is used. For example, $U = [\rho, \rho u_1, \rho u_2, \rho u_3, \mathcal{E}]^T$ is the the vector of dependent variables, E_i is a flux, $\overline{U} = U/J$, $\overline{E}_i = (\partial\xi_i/\partial x_j)E_j/J$, and J is the Jacobian of the grid transformation. The metrics were evaluated using the method of Thomas and Lombard.[75]

Writing Eq. (6) as $\partial\overline{U}/\partial t = R$, and discretizing in time, we have:

$$\frac{(1+\theta)\overline{U}^{n+1} - (1+2\theta)\overline{U}^{n} + \theta\overline{U}^{n-1}}{\Delta t} = R^{n+1} \tag{7}$$

where $\theta = 0$ for an implicit Euler scheme and $\theta = 1/2$ for a three point backward scheme. We introduce subiterations such that $\overline{U}^{n+1} \rightarrow \overline{U}^{p+1}$, with $\Delta\overline{U} = \overline{U}^{p+1} - \overline{U}^{p}$. The right hand side R^{n+1} is linearized in the standard thin layer manner. Collecting the implicit terms on the left hand side, and introducing approximate factoring and a subiteration time step $\Delta\hat{t}$ gives:

$$\mathcal{L}_1\mathcal{L}_2\mathcal{L}_3\ \Delta\overline{U} = -\frac{\Delta\hat{t}}{1+\theta}\left\{\frac{(1+\theta)\overline{U}^{p} - (1+2\theta)\overline{U}^{n} + \theta\overline{U}^{n-1}}{\Delta t} - R^p\right\} \tag{8}$$

where $\mathcal{L}_i$ is a derivative operator containing source and flux Jacobians. The implicit terms were evaluated using the scalar pentadiagonal formulation of Pulliam and Chaussee.[76] Equation (8) was solved at each subiteration, driving $\Delta\overline{U}$ to zero. The spatial derivatives on the left-hand-side are evaluated using second-order central differences, and the operators incorporate the implicit damping approach described by Pulliam.[73]

The spatial differencing scheme for the right-hand-side was based on compact differencing.[70,77,78] In one dimension, the finite difference approximation to the first derivative ϕ'_i is evaluated by solving a tridiagonal system of the form:

$$\alpha\phi'_{i-1} + \phi'_i + \alpha\phi'_{i+1} = a\,\frac{\phi_{i+1} - \phi_{i-1}}{2} + b\,\frac{\phi_{i+2} - \phi_{i-2}}{4} \tag{9}$$

where α, a, and b are constants chosen to give a certain order of accuracy and set of spectral properties for the scheme. Second derivatives were found by applying the first derivative operator twice. In the present work, a sixth-order scheme was used for interior points, dropping to fifth- and fourth-order approaching boundaries.

Numerical stability was enforced using a low-pass, Padé-type, non-dispersive spatial filter.[70,78] The filtering approach replaces the computed value ϕ_i at a particular node with a filtered value $\overline{\phi}_i$:

$$\alpha_f \overline{\phi}_{i-1} + \overline{\phi}_i + \alpha_f \overline{\phi}_{i+1} = \sum_{n=0}^{N} \frac{a_n}{2} (\phi_{i+n} + \phi_{i-n}) \tag{10}$$

where the constants α_f, a_0, ... a_N are chosen to give appropriate filter properties. The filter was applied to the solution vector, sequentially, in each of the three computational directions, following each sub-iteration in implicit time integration. The order of the filtering operation was permuted at each time step. For the computations presented here, an eighth-order filter with $\alpha_f = 0.40$ was employed for interior points. Near boundaries, the filter order was dropped in steps of 2, with no filtering of the boundary points. The filter coefficient was increased gradually to $\alpha_f = 0.49$ at the first point off the boundary.

The code's capabilities include the shock capturing method of Visbal and Gaitonde.[71] In this approach, a simple detector, based on a WENO smoothness criterion, is used to identify discontinuities, and the numerical scheme is reduced to a third-order upwind-biased Roe scheme for the cells in the vicinity of a shock. This feature was only employed for the Mach 4.9 turbulent boundary layer flow discussed in Sec. III.B.

In the implementation of the computer code, multi-level parallelism is exploited by using vectorization, multi-threading with OpenMP commands,[79] and multi-block decomposition implemented through MPI commands.[80] Typical runs on the largest grid were carried out by decomposing the domain into blocks of $141^3 \approx 2.8 \times 10^6$ points, each executed with an MPI task and up to eight OpenMP threads. Additional details on these aspects of the implementation were reported in an earlier paper.[61]

The largest computations (Grids 4 and 5, discussed below) were executed on 23040–46080 cores on the SGI ICE X supercomputer Spirit at AFRL, and on 46080–102400 cores on the Cray XE6 supercomputer Garnet at ERDC.

C. Flowfield

The present work investigated flat plate turbulent boundary layer flows. The baseline case was a flow at Mach 2.3, under conditions similar to those employed in several previous numerical investigations.[27,32,33,81] The flow conditions are listed in Table 2. The baseline case corresponds to the adiabatic wall temperature, $T_w = T_{aw}$ (see Sec. III.A). Additional calculations (see Sec. III.B) were carried out with different wall temperatures: $T_w = 0.52\,T_{aw}$ ($T_w = T_\infty$) and $T_w = 2.0\,T_{aw}$. A near-adiabatic wall case at Mach 4.9 was also considered; the conditions are listed in Table 3.

The notation used here is that x_1 is the coordinate in the streamwise direction, x_2 is the wall-normal coordinate, and x_3 is spanwise. In each case, the computational domain was a rectangular box, with the wall at the bottom ($x_2 = 0$) and periodic boundary conditions at the sides (x_3-direction). The size of the resolved region corresponds to $L_1 = 100\delta_0$ by $L_2 = 5\delta_0$ by $L_3 = 5\delta_0$, where δ_0 is the initial boundary layer thickness. A region of grid stretching (25 points) was added in the x_1- and x_2-directions to support the outflow boundary conditions at the top and the end of the domain. A small overlap region (5 points) in the x_3-direction was added to enforce periodicity.

The inflow boundary condition was provided by a similarity solution of the compressible, laminar boundary layer equations.[69] The inflow profiles used for each case are shown in Fig. 1. No-slip conditions were imposed on the flat-plate surface, with zero wall-normal pressure gradient.

Transition to turbulent flow was promoted using a body-force trip method.[82] An artificial body force f_i was added to the momentum equation (2), and its corresponding work $f_j u_j$ was added to the total energy equation (3). The magnitude of this body force was taken to be:

$$f = \frac{2D_c}{\pi \ell_1 \ell_2 \ell_3} \sin^2\left(\pi \frac{x_3 - X_3}{\ell_3}\right) \exp\left[-\left(\frac{x_1 - X_1}{\ell_1}\right)^2 - \left(\frac{x_2 - X_2}{\ell_2}\right)^2\right] \tag{11}$$

The smooth variation in the form of the trip function obviated the need for grid clustering around the trip, and the sinusoidal variation in the spanwise direction was found to promote more rapid transition.

(Previous work[67] used a force distribution for the trip that was triangular in the x_1-x_2-plane, and uniform in the spanwise direction.) The components of the force were:

$$\begin{aligned} f_1 &= f\cos\theta \\ f_2 &= f\sin\theta \\ f_3 &= 0 \end{aligned} \tag{12}$$

Typical parameters were chosen to be $X_1 = 2.5\,\delta_0$, $X_2 = 0$, $X_3 = 0$, $\ell_1 = 0.17\,\delta_0$, $\ell_2 = 0.01\,\delta_0$, $\ell_3 = 0.5\,\delta_0$, $\theta = 179$ deg, and $D_c = 1.5 \times 10^{-2}$. (Here δ_0 is the thickness of the laminar boundary layer imposed at the inflow boundary.) For this choice of parameters, only the $x_2 \geq 0$ half of the force magnitude distribution, Eq. (11), acts on the flow.

Each calculation was carried out with a nondimensional time step of $U_\infty \Delta t/\delta_0 = 5 \times 10^{-3}$, corresponding to a time step in inner units of $\Delta t^+ = 5 \times 10^{-2}$ for the baseline Mach 2.3 flow. A previous paper[68] showed that calculations employing a time step in this range are well resolved. An initial run to allow the solution to reach a statistically steady state was executed for at least 60000 time steps, that is, for $U_\infty T/\delta_0 = 300$ or three flow-through times for the domain. Statistics were recorded for at least 60000 additional iterations.

To minimize storage requirements for the larger computations, a limited subset of the data was recorded for statistical analysis. The plane $x_1/\delta_0 = 100$ was saved every 200 iterations, and a spanwise line at the boundary layer half-height ($x_1/\delta_0 = 100$, $x_2/\delta = 0.5$) was recorded for every time step. For the smaller calculations, data from the $x_2 = 0$ and $x_3/\delta_0 = 2.5$ planes were also saved.

D. Signal Analysis

To be consistent with experimental practice, the spectra and correlations were processed using the procedures described by Bendat and Piersol.[83] For the auto-spectra, the data were windowed and tapered with the Hanning window to avoid side-lobe leakage, and averaged using 50% overlap. For the auto-correlations, the data were windowed with no overlap, and zero-padded. Tapering and zero-padding were not used for periodic data in the present work, that is, for functions of the spanwise, x_3-direction.

To avoid aliasing, an analog low-pass filter, with a cut-off at the Nyquist frequency $f_c = 1/(2\Delta t)$, must be applied to experimental data before digitization. A stable numerical scheme obviates the need for this procedure in a simulation by suppressing small-scale oscillations. In general, the numerical results are over-resolved in time. For example, the time step for the baseline Mach 2.3 flow was $\Delta t^+ = 5.3 \times 10^{-2}$, so the Nyquist frequency in inner units was $f_c^+ = 9.4$, a region of the spectrum where there is almost no detectable energy.

For the temporal spectra and correlations, data were collected in windows of 10000 points, corresponding to $U_\infty T/\delta_0 = 50.0$. For the spanwise correlations and wavenumber spectra, the window size corresponded to the number of points in the span, less the 5 overlap points. Thus, the spanwise window size was 112–1126 points.

III. Results

Two main projects were carried out in this work. First, the effects of spatial resolution on spectra and other flow statistics were examined for the baseline Mach 2.3 turbulent boundary layer flow. This work is presented in Sec. III.A. Second, variations from the baseline flow conditions were considered, and the results compared to the turbulence model of Bowersox.[52] Results of this second project are reported in Sec. III.B.

A. Effects of Spatial Resolution

Table 2 shows the flow conditions for the calculations, and Tables 4–5 show the mesh size and spatial resolution of each grid. Grid 1 meets the requirements for wall-resolving implicit large-eddy simulation, and Grids 2–4 lie in a regime usually accepted as direct numerical simulation.[50] Grid 5 should correspond to direct numerical simulation in the strictest sense. Employing 3.3×10^{10} points, this grid maintains $\max(\Delta x_1^+, \Delta x_2^+, \Delta x_3^+) \leq 1$ everywhere. For comparison, the minimum value of the Kolmogorov length scale occurs at the wall, and has a value of $\eta^+ \approx 1.5$ (see Pope,[84] p. 287).

Figure 2 presents a sample of the solution obtained on Grid 5. The field of view corresponds to $95 \leq x_1/\delta_0 \leq 100$, $0 \leq x_2/\delta_0 \leq 5$, and $0 \leq x_3/\delta_0 \leq 5$. The local boundary layer thickness is about $\delta = 2.5\delta_0$,

so the field of view is a cube about 2δ on a side situated at the end of the resolved region of the mesh. At this high level of resolution, the solution looks remarkably like experimental laser scattering visualization of supersonic, turbulent boundary layer flows.[18,19,85] High-density, freestream fluid often penetrates close to the wall (as close as $x_2/\delta = 0.05$ here), and low-density boundary layer fluid is often ejected past the mean boundary layer edge (here as far as $x_2/\delta = 1.2$). A distinct, large-scale structure angle of about 45 deg is evident in the outer part of the the boundary layer, and a shallower angle of about 10 deg is apparent closer to the wall.

Figure 3 shows samples of the instantaneous density field in the $x_1/\delta_0 = 100$ plane for Grid 1 (HFILES) and Grid 5 (DNS). This view corresponds to the end-plane of the resolved region of the computational domain; flow is into the page. The effect of resolution is very apparent. Motions in the outer layer are highly smeared in the coarse grid case, whereas the fine grid captures the sharp vortical-irrotational interface of the viscous superlayer.[7]

Figure 4 shows the effect of spatial resolution on turbulent boundary layer profiles at $x_1/\delta_0 = 100$. Profiles of the mean streamwise velocity are shown in outer coordinates in Fig. 4a. These profiles are seen to collapse closely for Grids 2–5. Grid 1 appears to produce a transitional boundary layer flow. This is probably a result of slow streamwise development with the coarse streamwise resolution; better results would probably be obtained for this level of resolution on a longer streamwise domain.

Figure 4b shows mean velocity profiles in van Driest-transformed inner coordinates for Grids 3–5. Following Guarini et al.,[28] the composite inner layer profile of Reichardt[86] and Finley et al. is shown for comparison:

$$u^+ = C_1 \left(1 - e^{-x_2^+/\eta_1} - \frac{x_2^+}{\eta_1} e^{-bx_2^+}\right) + \frac{1}{\kappa}\ln(1+\kappa x_2^+) + \frac{1}{\kappa}\left[(1+6\Pi)\left(\frac{x_2}{\delta}\right)^2 - (1+4\Pi)\left(\frac{x_2}{\delta}\right)^3\right] \tag{13}$$

Here $\eta_1 = 11$, $b = 33$, $C_1 = 7.1$, $\kappa = 0.41$, and $\Pi = 0.54$. Also shown are the experimental measurements of Éléna et al.[87] The discrepancy between computation and experiment is within the experimental uncertainty, which is about the size of the symbols on this plot.

Figure 4c shows profiles of the Reynolds normal stress $\rho\overline{u'^2}$ for the simulations ($M = 2.3$, $\mathrm{Re}_{\theta i} = 2.0\times10^3$, Grids 3–5) and the experiments of Alving[88] ($M \approx 0$, $\mathrm{Re}_\theta = 5.0\times10^3$), Éléna and Lacharme[87] ($M = 2.3$, $\mathrm{Re}_{\theta i} = 2.6\times10^3$), and Konrad[89] ($M = 2.9$, $\mathrm{Re}_{\theta i} = 3.6\times10^4$) . As expected for a plot in outer coordinates, the experimental data collapse approximately onto a common curve for $x_2/\delta > 0.2$. The computational results agree with this curve, within the reported experimental error.

Convergence of the Reynolds normal stress with grid resolution is illustrated in Fig. 4d, which shows the $\rho\overline{u_1'^2}$ profile in inner coordinates. Differences in the peak Reynolds stress are seen for Grids 1 and 2, but the data collapse nicely for Grids 3–5.

According to Corrsin and Kistler,[7] the viscous superlayer, or boundary between irrotational and turbulent fluid, is on the order of the Kolmogorov length scale in thickness. This small scale feature may thus be sensitive to numerical resolution near the boundary layer edge. Statistics characterizing the superlayer were analyzed to examine this possibility.

A density contour near the freestream value has often been used experimentally as a surrogate for the vortical-irrotational interface.[90] Here we examine the intermittency and probability density functions (PDFs) of the density. The PDF of density is bimodal in the outer part of the boundary layer, with a minimum at $\rho \approx 0.975\rho_\infty$. The intermittency was thus defined with this value as the threshold: $\gamma = P[\rho < 0.975\rho_\infty]$. In other words, the intermittency is the probability that the density is less than 97.5% of the freestream density.

The intermittency profile is shown in Fig. 5a. As found in previous studies,[7,11] the profile has the shape of an error function, or cumulative normal distribution. Thus the location of the superlayer has a normal (Gaussian) distribution, centered around $y/\delta = 0.9$ where $\gamma \approx 0.5$. The PDF for that station in the boundary layer is shown in Fig. 5b. Both the intermittency profile and the probability density function are seen to be relatively insensitive to grid resolution near the boundary layer edge. The statistics of superlayer location seem to be primarily fixed by large-scale boundary layer structures.

A comparison of the intermittency computed for Grid 5 to experimental data is shown in Fig. 5c. The experimental intermittency is derived from hotwire measurements[7,11,91] and from the vaporization boundary in condensate-enhanced Rayleigh scattering.[19] The shape of the curves is seen to be nearly identical. The differences between the results are primarily a result of the choice of threshold in computing intermittency. (There is no standard value in the literature for this threshold.)

Another way of characterizing intermittency is through the fractal dimension of the viscous superlayer.[90] The fractal dimension of an object embedded in a two-dimensional space can be efficiently estimated using the box-counting algorithm. Here a planar region is tiled with boxes of size r, and the number of boxes N that contain the boundary is counted. For a self-similar fractal, this number is $N(r) \propto r^{-D_2}$, where D_2 is the fractal dimension.

The fractal dimension can be viewed as a measure of the degree with which the fractal fills space; the value lies in the range $1 \leq D_2 < 2$. For a smooth, geometric shape, like a square, the fractal dimension is the same as the Euclidean dimension of the boundary: $D_2 = 1$. Through an argument based on dimensional analysis and Reynolds number independence, Sreenivasan et al.[92] predicted that $D_2 = 4/3$ for the boundary layer vortical-irrotational interface at high Reynolds number. This prediction has been corroborated by flow visualization experiments, with caveat that results obtained with a laser sheet thicker than the Kolmogorov scale tend display artificially low fractal dimension due to spatial averaging.

The box counting algorithm was applied to the $0.975\rho_\infty$ contour for the data on each of the grids. The results were averaged over about 300 realizations, and are shown on a log-log plot in Fig. 5d. The computational results are seen to lie on the predicted $-4/3$ slope for large scales, and change to -1 slope at small scale. This result is exactly as expected: the interface looks smooth when viewed on small scales. Interestingly, grid resolution in the range considered here has little effect on the fractal dimension at large scale. Filtering merely smooths out some of the small scale content.

A very strict test of spatial convergence of a turbulent flow simulation is comparison of computed velocity spectra on different grids.[25] A large body of spectral measurements in low-speed turbulent boundary layers is available in the literature. Since Morkovin's hypothesis[21] is expected to apply for $M = 2.3$, these data should be suitable for comparison to the present calculations. Saddoughi and Veeravalli[93] measured velocity spectra in a low Mach number, high Reynolds number turbulent boundary layer, and compared the results to a variety of experiments spaning the range $R_\lambda = 23$ to 3180 ($\mathrm{Re}_L = 79$ to 1.52×10^6). (Here R_λ is the Reynolds number based on the Taylor microscale, and $\mathrm{Re}_L = (k^T)^2/(\epsilon\nu) = 3R_\lambda^2/20$ is the turbulence Reynolds number.)

Pope[84] (pp. 232–234) proposed a semi-empirical model of the velocity spectrum of isotropic turbulence that is in excellent agreement with the experimental data presented by Saddoughi and Veeravalli. The energy spectrum function $E(\kappa)$ has the following properties. The integral over all wavenumbers $\kappa = 2\pi/\lambda$ is equal to the turbulent kinetic energy:

$$k^T = \int_0^\infty E(\kappa)\, d\kappa \tag{14}$$

and the second moment of the energy spectrum function is proportional to the dissipation:

$$\epsilon = 2\nu \int_0^\infty \kappa^2 E(\kappa)\, d\kappa \tag{15}$$

Pope's model has the following form:

$$\begin{aligned} E(\kappa) &= C\, \epsilon^{2/3}\kappa^{-5/3}\, f_L(\kappa L)\, f_\eta(\kappa\eta) \\ f_L(\kappa L) &= \left[\frac{\kappa L}{\sqrt{(\kappa L)^2 + c_L}}\right]^{5/3+p_0} \\ f_\eta(\kappa\eta) &= \exp\left(-\beta\left\{\left[(\kappa\eta)^4 + c_\eta^4\right]^{1/4} - c_\eta\right\}\right) \end{aligned} \tag{16}$$

where $p_0 = 2$, $C = 1.5$, and $\beta = 5.2$. The remaining constants c_L and c_η are determined for a given Reynolds number by satisfying Eqs. (14)–(15). For the present work, these values were obtained numerically using integration of the spectra with the trapezoidal rule, and applying quasi-Newton iteration to solve the resulting two nonlinear equations for c_L and c_η. Figure 6a shows the model $E(\kappa)$ spectrum for different values of the turbulence Reynolds number Re_L. (Note that $\kappa L = \kappa\eta\, \mathrm{Re}_L^{3/4}$.)

The corresponding one-dimensional, longitudinal spectrum (see Pope,[84] pp. 226–227) can be determined from the following integral:

$$E_{11}(\kappa_1) = \int_{\kappa_1}^\infty \frac{E(\kappa)}{\kappa}\left(1 - \frac{\kappa_1^2}{\kappa^2}\right) d\kappa \tag{17}$$

This integral was evaluated for the model spectrum using the trapezoidal rule, and is plotted in Fig. 6b. The flat spectrum at low wavenumber in Fig. 6b is a result of aliasing in the conversion from the three-dimensional

spectrum to one-dimensional spectrum. Under the assumption of isotropy, the spectra $E_{11}(\kappa_1)$ and $E_{33}(\kappa_3)$, which will be examined below, have the same form.

Computational results on the different grids were compared to Pope's model spectrum. To convert the computational results to the appropriate nondimensional variables, integrals of the following form were evaluated for each spectrum:

$$\begin{aligned} k^T &= \frac{3}{2}\int_0^\infty E_{11}(\kappa_1)\, d\kappa_1 \\ \epsilon &= 15\nu \int_0^\infty \kappa_1^2 E_{11}(\kappa_1)\, d\kappa_1 \end{aligned} \tag{18}$$

Data from local conditions were employed in all the calculations. For the temporal spectra, Taylor's hypothesis was applied to convert frequency to streamwise wavenumber: $\kappa_1 = 2\pi f/U_c$. For the present flow, $U_c \approx 0.5\, u_1$ was found to provide a good match between the temporal spectra and the spanwise wavenumber spectra at $x_2/\delta = 0.5$.

Figure 7 shows the effect of spatial resolution in the computations on velocity spectra extracted at $x_1/\delta_0 = 100$, $x_2/\delta = 0.5$. In these plots, the wavenumber corresponding to the local Kolmogorov scale is $\kappa_i \eta = 2\pi \approx 6$. The black line is Pope's model spectrum. Based on Eq. (18), the Taylor microscale Reynolds number is $R_\lambda \approx 70$ and the turbulent Reynolds number is $\mathrm{Re}_L \approx 800$.

Results are presented for the spanwise wavenumber spectrum $E_{33}(\kappa_3)$ in Fig. 7a. As the spanwise grid resolution decreases from $\Delta x_3^+ = 10$ on Grid 2 to $\Delta x_3^+ = 1$ on Grid 5, the computational spectra converge smoothly to Pope's model spectrum. At lower frequencies there is agreement between all the curves, but at higher frequencies, the effect of spatial filtering is evident at a rapid drop-off in the magnitude of the spectrum on the coarser grids. Similar trends were observed by Rizzetta and Visbal[33] in a comparison of their wavenumber spectra to those of the better-resolved computation of Rai et al.[27] (See Fig. 7 of Ref. 33.)

Results are presented for the temporal spectrum $E_{11}(\kappa_1)$ in Fig. 7b. For the temporal domain, the computational spectra are again seen to converge to a close match to Pope's model spectrum as resolution is increased. In particular, smooth convergence and agreement at low wavenumber are seen for Grids 2–5. Results of marginal quality are obtained on Grid 1; this may be a result of the transitional state of this case (see Fig. 4a).

Additional calculations were carried out, maintaining the resolution of Grid 3, but varying the domain width over the range $L_3/\delta_0 = 5$, 10, 15, corresponding to $L_3/\delta = 2$, 4, 8, where δ_0 is the initial boundary layer thickness and δ is the local boundary layer thickness at $x_1/\delta_0 = 100$. Figure 8 shows samples of the instantaneous density field in the $x_1/\delta_0 = 100$ plane for each of the three cases. There is no qualitative difference between the cases. Further, the boundary layer thickness is the same, as are boundary layer profiles. (The plots are omitted for brevity; see Poggie.[68]).

Figure 9 shows the effect of varying domain width on the spanwise wavenumber spectra and the temporal spectra. (Compare with Fig. 7.) The spanwise wavenumber spectra (Fig. 9a) collapse perfectly at high wavenumber, and the only effect of additional domain width is to extend the spectrum at low wavenumber. Capturing this long-wavelength content in the spanwise direction may be of interest in the simulation of unsteady separation,[94] and warrants additional work. The temporal spectra (Fig. 9b) are indistinguishable on the three grids.

Figure 10 shows the effect of domain width on the auto-correlation of velocity R_{11}. The spanwise auto-correlation of velocity $R_{11}(x_3)$ (Fig. 10a) is quite small at the maximum spanwise separation: $R_{11} < 0.05$ for $x_3 = \delta$ on the baseline grid, and it is negligible on the wider grids. The temporal correlations $R_{11}(t)$ are indistinguishable on the three grids.

To summarize, basic turbulence statistics were converged for a grid resolution of $\Delta x_1^+ \leq 10$, $(\Delta x_2^+)_w < 1$, $(\Delta x_2^+)_e \leq 10$, $\Delta x_3^+ \leq 10$. The requirements for of the velocity spectra are more stringent, perhaps $\Delta x_1^+ \leq 2$, $(\Delta x_2^+)_w < 1$, $(\Delta x_2^+)_e \leq 2$, $\Delta x_3^+ \leq 1$ for strict convergence. A domain width of twice the maximum boundary layer thickness seen to be adequate, but probably should be considered the minimum acceptable width.

B. Turbulence Models, Wall Temperature, and Mach Number

A second project was undertaken to explore turbulent boundary layer physics in the context of turbulence modeling. Of particular interest was the turbulent energy flux, and the ability to accurately predict heat transfer rates. To explore a range of conditions relevant to high-speed flight, calculations were carried out at Mach 2.3 for different wall temperatures: $T_w = 0.52\, T_{aw}$, $1.0\, T_{aw}$, and $2.0\, T_{aw}$, and at Mach 4.9 for

$T_w = 0.93\,T_{aw}$. Dimensional flow conditions for the Mach 2.3 adiabatic wall case are given in Table 2; only the wall temperature was varied for the remaining supersonic cases. Flow conditions for the hypersonic Mach 4.9 case are listed in Table 3. Grid resolution was maintained at a level close to the Grid 3 case discussed in Sec. III.A. Details are given in Table 6.

Before comparing to the turbulence model, we examine the HFILES results over the range of flow conditions. Figure 11a shows profiles of the mean streamwise velocity in van Driest transformed[22] inner coordinates. As expected, there is reasonably good collapse in these coordinates for the inner region of the profile. Figure 11b shows profiles of the Reynolds normal stress $\rho\overline{u_1'^2}$ in outer coordinates. Again, relatively good collapse is obtained, supporting Morkovin's hypothesis.[21] Overall, the level of collapse of the data is similar to that obtained in previous studies of Mach number[41,43] and wall temperature[39] effects.

The two near-adiabatic wall cases, $M = 2.3$, $T_w/T_{aw} = 1.0$, $\delta^+ = 560$ and $M = 4.9$, $T_w/T_{aw} = 0.93$, $\delta^+ = 730$, had nearly matching Reynolds numbers. Thus a comparison of these two cases isolates the effects of Mach number alone. To this end, Fig. 12 shows correlations for these two cases. Figures 12a and 12c show correlations of the streamwise mass flux in an end-view plane ($x_1/\delta_0 = 90$), and Figs. 12b and 12d show pressure correlations at the wall ($x_2 = 0$). The change in Mach number has a relatively small effect. The correlation contours look very similar, with perhaps a slight reduction in length scale for the higher Mach number case.

The results of the simulations were compared to the turbulence model of Bowersox,[52,53] implemented in a boundary layer solver. This model emphasizes internal energy as the coupling mechanism between the kinematic and thermodynamic fluctuations. For simplicity in the present description of the model, we assume an ideal gas and ignore the difference between Reynolds-averaged and Favre-averaged variables. In the Reynolds-averaged equations of motion (see Gatski and Bonnet,[6] Sec. 3.3–3.4 and Smits and Dussauge,[5] Sec. 3.2), the two moments that require closure models are the turbulent energy flux $q_i^T = \rho\overline{h'u_i'}$ and the Reynolds stress $\tau_{ij}^T = -\rho\overline{u_i'u_j'}$.

First we consider the algebraic model for the energy flux. In the Bowersox model, the transport equation of the energy flux $\theta_i^T = \rho\overline{e'u_i'}$ was simplified to:

$$
\begin{aligned}
a_{ik}\theta_k^T &= b_i \\
a_{ik} &= \left[\frac{1}{\tau_\theta} + \frac{R}{C_v}\frac{\partial u_m}{\partial x_m}\right]\delta_{ik} + \frac{\partial u_i}{\partial x_k} \\
b_i &= \tau_{ik}^T\left(\frac{\partial h}{\partial x_k} - \frac{1}{\rho}\frac{\partial p}{\partial x_k}\right) + \frac{1}{\rho}\left(\tau_{kl}^T\frac{\partial u_l}{\partial x_k}\right)\frac{\partial p}{\partial x_i}\tau_e
\end{aligned}
\tag{19}
$$

Here, $\tau_\theta = \sigma_\theta\tau_u$ and $\tau_e = \sigma_e\tau_u$ are time scales. For a boundary layer flow, Eq. (19) reduces to:

$$
\begin{aligned}
\theta_1^T &= \tau_{12}^T\frac{\partial h}{\partial x_2}\tau_\theta - \tau_{22}^T\frac{\partial h}{\partial x_2}\frac{\partial u_1}{\partial x_2}\tau_\theta^2 \\
\theta_2^T &= \tau_{22}^T\frac{\partial h}{\partial x_2}\tau_\theta
\end{aligned}
\tag{20}
$$

For the present work, adjustable constant in the time scale $\tau_\theta = \sigma_\theta\tau_u$ taken to be $\sigma_\theta = 0.28/\gamma$. The turbulence time scale was defined to be $\tau_u = k^T/\epsilon$ as in the k–ϵ model,[95] and estimated as:

$$
\tau_u = \frac{a_1/C_\mu}{\partial u_1/\partial x_2} \tag{21}
$$

where $a_1 = 0.28$ and $C_\mu = 0.09$. At the present level of approximation, we use Eq. (20) to find θ_i^T, and find the turbulent energy flux as $q_i^T = \gamma\theta_i^T$.

As part of the approximation leading to Eq. (19), the following relation was used:

$$
\rho C_v\overline{T'^2} = -2\,\tau_{22}^T\left(\frac{\partial h}{\partial x_2}\right)^2\tau_\theta\tau_e \tag{22}
$$

where the time scale $\tau_e = \sigma_e\tau_u$ was computed using $\sigma_e = 0.72/\gamma$ and Eq. (21).

For simplicity, the Reynolds shear stress was computed using a traditional eddy viscosity model:

$$
\tau_{12}^T = \mu^T\frac{\partial u_1}{\partial x_2} \tag{23}
$$

The turbulent viscosity had the following form in the inner region:

$$\mu_i^T = \rho \left[\kappa x_2 \left(1 - e^{-x_2^+/A^+} \right) \right]^2 \left| \frac{\partial u_1}{\partial x_2} \right| \tag{24}$$

where $\kappa = 0.41$ and $A^+ = 26.0$. This is a mixing length model, employing the van Driest damping function.[22] In the outer region, the turbulent viscosity had the form:

$$\mu_o^T = \frac{C_C \, \rho U_e \delta_k^*}{1 + C_K \, (x_2/\delta)^{n_K}} \tag{25}$$

where $\delta_k^* = \int_0^\infty (1 - u_1/U_\infty) \, dx_2$ is the kinematic displacement thickness. Here $C_C = 0.018$, $C_K = 1.2$, and $n_K = 6.0$. Equation (25) corresponds to the Clauser[96] model with the Klebanoff[97] intermittency correction. A Klebanoff-type blending was used to smoothly merge Eqs. (24)-(25) at height of $x_2 = (C/\kappa)(U_e/u_\tau)\delta^*$. The Reynolds normal stress τ_{22}^T was computed from:

$$\frac{\tau_{12}^T}{\tau_{22}^T} = -\frac{C}{1 - e^{-x_2^+/A^+}} \tag{26}$$

where $C = 0.68$ and $A^+ = 26.0$.

A comparison of the predictions of the simulations and the turbulence model is given in Figs. 13–16. Figure 13 shows the mean streamwise velocity profiles in outer coordinates. Agreement between the two approaches is seen to be excellent in all cases. A similar level of agreement is seen in plots (Fig. 14) of the Reynolds shear stress $-\rho\overline{u_1' u_2'}$. Relative to the simulations, the turbulence model is seen to produce slightly lower values of the peak Reynolds stress.

The core of the Bowersox model is the prediction of the turbulent energy flux through the reduced form of the energy flux transport equation (19). Results for the streamwise and spanwise components of the energy flux are presented in Figs. 15–16 .

Figure 15 compares the streamwise turbulent energy flux $\rho\overline{u_1' T'}$ predicted by the large-eddy simulations to that predicted by the Bowersox model. For the cold wall case (Fig. 15a), this quantity is positive near the wall, but changes sign in the outer part of the boundary layer. For higher wall temperatures (Figs. 15b-d), $\rho\overline{u_1' T'} \leq 0$ across the whole profile.

A change of sign is also seen in the corresponding profiles of the transverse turbulent energy flux $\rho\overline{u_2' T'}$ (Figure 16). For the cold wall case (Figure 16a), the transverse energy flux is negative near the wall, and positive near the boundary layer edge. For the remaining cases, we find $\rho\overline{u_2' T'} \geq 0$ over the whole profile.

Figure 17 shows the intensity of temperature fluctuations $(\rho\overline{T'^2})^{1/2}$. The turbulence model employed Eq. (22) to predict this quantity. Interestingly, two maxima are present in these profiles. One occurs close to the wall, and the other near the boundary layer edge. The two peaks are most prominent in the cold-wall case.

It is impressive how well the algebraic energy flux model matches the large-eddy simulations for such low Reynolds numbers, and for such a wide range of wall temperatures. Even when there are quantitative differences, the curves match qualitatively. In particular, similar maxima and minima are present.

IV. Conclusions

Direct numerical simulations (DNS) and high-fidelity, implicit large-eddy simulations (HFILES) were carried out for turbulent boundary layers at Mach 2.3 and 4.9. Transition to turbulence was promoted with an artificial body force trip. Two main projects were carried out in the work reported here.

First, the effects of spatial resolution on spectra and other flow statistics were examined for a Mach 2.3, adiabatic wall, turbulent boundary layer flow. Examining velocity spectra in detail, HFILES was seen to converge seamlessly to DNS as the spatial resolution was increased. Further, turbulence statistics were found to be essentially independent of the domain width for values between two and eight times the maximum boundary layer thickness.

Second, variations from the baseline flow conditions were considered, and the results compared to an algebraic model for the energy flux developed by R. Bowersox. An impressive match was obtained between the model and simulations, for a wide range of wall temperature and Mach number.

Acknowledgments

This project was sponsored in part by the Air Force Office of Scientific Research, under LRIR Task 14RQ18COR monitored by I. Leyva. It was also supported by grants of High Performance Computing time from the Department of Defense Supercomputing Resource Centers at the Air Force Research Laboratory, the Army Research Laboratory, and the Army Engineer Research and Development Center, provided under a Department of Defense, High-Performance Computation Modernization Program Frontier Project.

The work presented in Sec. III.A was carried out in collaboration with N. Bisek and R. Gosse under the Frontier Project. The work presented in Sec. III.B was carried out in collaboration with R. Bowersox under AFOSR sponsorship.

References

[1]Boris, J. P., Grinstein, F. F., Oran, E. S., and Kolbe, R. L., "New Insights into Large Eddy Simulation," *Fluid Dynamics Research*, Vol. 10, No. 4–6, 1992, pp. 199–228.

[2]Visbal, M. R. and Rizzetta, D. P., "Large-Eddy Simulation on Curvilinear Grids Using Compact Differencing and Filtering Schemes," *Journal of Fluids Engineering*, Vol. 124, No. 4, 2002, pp. 836–847.

[3]Robinson, S. K., "Coherent Motions in the Turbulent Boundary Layer," *Annual Review of Fluid Mechanics*, Vol. 23, 1991, pp. 601–639.

[4]Spina, E. F., Smits, A. J., and Robinson, S. K., "The Physics of Supersonic Turbulent Boundary Layers," *Annual Review of Fluid Mechanics*, Vol. 26, 1994, pp. 287–319.

[5]Smits, A. J. and Dussauge, J.-P., *Turbulent Shear Layers in Supersonic Flow*, Springer, New York, 2nd ed., 2006.

[6]Gatski, T. B. and Bonnet, J.-P., *Compressibility, Turbulence and High Speed Flow*, Elsevier, Amsterdam, 2nd ed., 2013.

[7]Corrsin, S. and Kistler, A. K., "Free-Stream Boundaries of Turbulent Flow," Technical Report NACA-TR-1244, National Advisory Committee for Aeronautics, January 1955.

[8]Hussain, A. K. M. F., "Coherent Structures – Reality and Myth," *Physics of Fluids*, Vol. 26, No. 10, 1983, pp. 2816–2850.

[9]Kline, S. J., Reynolds, W. C., Schraub, F. A., and Runstadler, P. W., "The Structure of Turbulent Boundary Layers," *Journal of Fluid Mechanics*, Vol. 30, 1967, pp. 741–773.

[10]Offen, G. R. and Kline, S. J., "A Proposed Model of the Bursting Process in Turbulent Boundary Layers," *Journal of Fluid Mechanics*, Vol. 70, 1975, pp. 209–228.

[11]Kovasznay, L. S. G., Kibens, V., and Blackwelder, R. F., "Large-Scale Motion in the Intermittent Region of a Turbulent Boundary Layer," *Journal of Fluid Mechanics*, Vol. 41, 1970, pp. 283–325.

[12]Owen, F. K. and Horstman, C. C., "On The Structure of Hypersonic Turbulent Boundary Layers," *Journal of Fluid Mechanics*, Vol. 53, 1972, pp. 611–636.

[13]Spina, E. F. and Smits, A. J., "Organized Structures in a Compressible, Turbulent Boundary Layer," *Journal of Fluid Mechanics*, Vol. 182, 1987, pp. 85–109.

[14]Spina, E. F., Donovan, J. F., and Smits, A. J., "On the Structure of High-Reynolds-Number Supersonic Turbulent Boundary Layers," *Journal of Fluid Mechanics*, Vol. 222, 1991, pp. 293–327.

[15]Smith, D. R. and Smits, A. J., "Simultaneous Measurement of Velocity and Temperature Fluctuations in the Boundary Layer of a Supersonic Flow," *Experimental Thermal and Fluid Science*, Vol. 7, No. 3, 1993, pp. 221–229.

[16]Tichenor, N. R., Humble, R. A., and Bowersox, R. D. W., "Response pf a Hypersonic Turbulent Boundary Layer to Favorable Pressure Gradients," *Journal of Fluid Mechanics*, Vol. 722, 2013, pp. 187–213.

[17]Beresh, S. J., Henfling, J. F., Spillers, R. W., and Pruett, B. O. M., "Fluctuating Wall Pressures Measured Beneath a Supersonic Turbulent Boundary Layer," *Physics of Fluids*, Vol. 23, 2011, pp. 075110.

[18]Smith, M. W. and Smits, A. J., "Visualization of the Structure of Supersonic Turbulent Boundary Layers," *Experiments in Fluids*, Vol. 18, 1995, pp. 288–302.

[19]Poggie, J., Erbland, P. J., Smits, A. J., and Miles, R. B., "Quantitative Visualization of Compressible Turbulent Shear Flows using Condensate-Enhanced Rayleigh Scattering," *Experiments in Fluids*, Vol. 37, 2004, pp. 438–454.

[20]Bradshaw, P., "Compressible Turbulent Shear Layers," *Annual Review of Fluid Mechanics*, Vol. 9, 1977, pp. 33–52.

[21]Morkovin, M. V., "Effects of Compressibility on Turbulent Flows," *Méchanique de la Turbulence*, edited by A. Favre, CNRS, Paris, France, 1962, pp. 367–380.

[22]van Driest, E. R., "On the Turbulent Flow Near a Wall," *Journal of the Aeronautical Sciences*, Vol. 23, 1956, pp. 1007–1011.

[23]Smits, A. J., Spina, E. F., Alving, A. E., Smith, R. W., Fernando, E. M., and Donovan, J. F., "A Comparison of the Turbulence Structure of Subsonic and Supersonic Boundary Layers," *Physics of Fluids*, Vol. 1, No. 11, 1989, pp. 1865–1875.

[24]Papamoschou, D., "Evidence of Shocklets in a Counterflow Supersonic Shear Layer," *Physics of Fluids*, Vol. 7, 1995, pp. 233–235.

[25]Coleman, G. N., Kim, J., and Moser, R. D., "A Numerical Study of Turbulent Supersonic Isothermal-Wall Channel Flow," *Journal of Fluid Mechanics*, Vol. 305, 1995, pp. 159–183.

[26]Huang, P. G., Coleman, G. N., and Bradshaw, P., "Compressible Turbulent Channel Flows: DNS Results and Modelling," *Journal of Fluid Mechanics*, Vol. 305, 1995, pp. 185–218.

[27]Rai, M. M., Gatski, T. B., and Erlebacher, G., "Direct Simulation of Spatially Evolving Compressible Turbulent Boundary Layers," AIAA Paper 95-583.

[28]Guarini, S. E., Moser, R. D., Shariff, K., and Wray, A., "Direct Numerical Simulation of a Supersonic Turbulent Boundary Layer at Mach 2.25," *Journal of Fluid Mechanics*, Vol. 414, 2000, pp. 1–33.

[29]Maeder, T., Adams, N. A., and Kleiser, L., "Direct Simulation of Supersonic Turbulent Boundary Layers by an Extended Temporal Approach," *Journal of Fluid Mechanics*, Vol. 429, 2001, pp. 187–216.

[30]Urbin, G. and Knight, D., "Large-Eddy Simulation of a Supersonic Boundary Layer Using an Unstructured Grid," *AIAA Journal*, Vol. 39, No. 7, 2001, pp. 1288–1295.

[31]Stolz, S. and Adams, N. A., "Large-eddy Simulation of High-Reynolds-Number Supersonic Boundary Layers Using the Approximate Deconvolution Model and a Rescaling and Recycling Technique," *Physics of Fluids*, Vol. 15, No. 8, 2003, pp. 2398–2412.

[32]Pirozzoli, S., Grasso, F., and Gatski, T. B., "Direct Numerical Simulation and Analysis of a Spatially Evolving Supersonic Turbulent Boundary Layer at $M = 2.25$," *Physics of Fluids*, Vol. 16, No. 3, 2004, pp. 530–545.

[33]Rizzetta, D. P. and Visbal, M. R., "Large-Eddy Simulation of Supersonic Boundary-Layer Flow by a High-Order Method," *International Journal of Computational Fluid Dynamics*, Vol. 18, No. 1, 2004, pp. 15–27.

[34]Sagaut, P., Garnier, E., Tromeur, E., Larchevêque, L., and Labourasse, E., "Turbulent Inflow Conditions for Large-Eddy Simulation of Compressible Wall-Bounded Flows," *AIAA Journal*, Vol. 42, No. 3, 2004, pp. 469–477.

[35]Xu, S. and Martin, M. P., "Assessment of Inflow Boundary Conditions for Compressible Turbulent Boundary Layers," *Physics of Fluids*, Vol. 16, No. 7, 2004, pp. 2623–2639.

[36]Martín, M. P., "Direct Numerical Simulation of Hypersonic Turbulent Boundary Layers. Part 1. Initialization and Comparison with Experiments," *Journal of Fluid Mechanics*, Vol. 570, 2007, pp. 347–364.

[37]Pirozzoli, S., Bernardini, M., and Grasso, F., "Characterization of Coherent Vortical Structures in a Supersonic Turbulent Boundary Layer," *Journal of Fluid Mechanics*, Vol. 613, 2008, pp. 205–231.

[38]Ringuette, M. J., Wu, M., and Martín, M. P., "Coherent Structures in Direct Numerical Simulation of Turbulent Boundary Layers at Mach 3," *Journal of Fluid Mechanics*, Vol. 594, 2008, pp. 59–69.

[39]Duan, L., Beekman, I., and Martín, M. P., "Direct Numerical Simulation of Hypersonic Turbulent Boundary Layers. Part 2. Effect of Wall Temperature," *Journal of Fluid Mechanics*, Vol. 655, 2010, pp. 419–445.

[40]Bernardini, M. and Pirozzoli, S., "Wall Pressure Fluctuations beneath Supersonic Turbulent Boundary Layers," *Physics of Fluids*, Vol. 23, 2011, pp. 085102.

[41]Duan, L., Beekman, I., and Martín, M. P., "Direct Numerical Simulation of Hypersonic Turbulent Boundary Layers. Part 3. Effect of Mach Number," *Journal of Fluid Mechanics*, Vol. 672, 2011, pp. 245–267.

[42]Duan, L., Beekman, I., and Martín, M. P., "Direct Numerical Simulation of Hypersonic Turbulent Boundary Layers. Part 4. Effect of high enthalpy," *Journal of Fluid Mechanics*, Vol. 684, 2011, pp. 25–59.

[43]Lagha, M., Kim, J., Eldredge, J. D., and Zhong, X., "A Numerical Study of Compressible Turbulent Boundary Layers," *Physics of Fluids*, Vol. 23, 2011, pp. 015106.

[44]Pirozzoli, S., "Numerical Methods for High-Speed Flows," *Annual Review of Fluid Mechanics*, Vol. 43, 2011, pp. 163–194.

[45]Di Marco, A., Camussi, R., Bernardini, M., and Pirozzoli, S., "Wall Pressure Coherence in Supersonic Turbulent Boundary Layers," *Journal of Fluid Mechanics*, Vol. 732, 2013, pp. 445–456.

[46]Pirozzoli, S. and Bernardini, M., "Probing High-Reynolds Number Effects in Numerical Boundary Layers," *Physics of Fluids*, Vol. 25, 2013, pp. 021704.

[47]Lund, T. S., Wu, X., and Squires, K. D., "Generation of Turbulent Inflow Data for Spatially-Developing Boundary Layer Simulations," *Journal of Computational Physics*, Vol. 140, 1998, pp. 233–258.

[48]Spina, E. F., *Organized Structures in a Supersonic Turbulent Boundary Layer*, Ph.D. Dissertation, Princeton University, Princeton NJ, October 1988.

[49]Ganapathisubramani, B., Clemens, N. T., and Dolling, D. S., "Large-Scale Motions in a Supersonic Turbulent Boundary Layer," *Journal of Fluid Mechanics*, Vol. 556, 2006, pp. 271–282.

[50]Georgiadis, N. J., Rizzetta, D. P., and Fureby, C., "Large-Eddy Simulation: Current Capabilities, Recommended Practices, and Future Research," *AIAA Journal*, Vol. 48, No. 8, 2010, pp. 1772–1784.

[51]Choi, H. and Moin, P., "Grid-Point Requirements for Large Eddy Simulation: Chapman's Estimates Revisited," *Physics of Fluids*, Vol. 24, 2012, pp. 011702.

[52]Bowersox, R. D., "Extension of Equilibrium Turbulent Heat Flux Models to High-Speed Shear Flows," *Journal of Fluid Mechanics*, Vol. 633, 2009, pp. 61–70.

[53]Bowersox, R. D. W. and North, S. W., "Algebraic Turbulent Energy Flux Models for Hypersonic Shear Flows," *Progress in Aerospace Sciences*, Vol. 46, 2010, pp. 49–61.

[54]Poggie, J. and Gaitonde, D. V., "Electrode Boundary Conditions in Magnetogasdynamic Flow Control," AIAA Paper 2002-0199.

[55]Sternberg, N. and Poggie, J., "Plasma-Sheath Transition in the Magnetized Plasma-Wall Problem for Collisionless Ions," *IEEE Transactions on Plasma Science*, Vol. 32, No. 6, 2004, pp. 2217–2226.

[56]Poggie, J., "Numerical Exploration of Flow Control with Glow Discharges," AIAA Paper 2004-2658.

[57]Poggie, J. and Sternberg, N., "Transition from the Constant Ion Mobility Regime to the Ion-Atom Charge-Exchange Regime for Bounded Collisional Plasmas," *Physics of Plasmas*, Vol. 12, No. 023502, 2005.

[58]Poggie, J., "Computational Studies of High-Speed Flow Control with Weakly-Ionized Plasma," AIAA Paper 2005-0784.

[59]Poggie, J., "Numerical Simulation of Direct Current Glow Discharges for High-Speed Flow Control," *Journal of Propulsion and Power*, Vol. 24, No. 5, 2008, pp. 916–922.

[60]Poggie, J., "Discharge Modeling for Flow Control Applications," AIAA Paper 2008-1357.

[61]Poggie, J., "Control of Shock-Wave / Boundary-Layer Interaction Using Volumetric Energy Deposition," AIAA Paper 2008-1090.

[62]Poggie, J., "High-Order Compact Difference Methods for Glow Discharge Modeling," AIAA Paper 2009-1047.

[63]Poggie, J., "Compact Difference Methods for Discharge Modeling in Aerodynamics," AIAA Paper 2009-3908.

[64]Poggie, J., "Role of Charged Particle Inertia in Pulsed Electrical Discharges," AIAA Paper 2010-1195.

[65]Poggie, J., "High-Order Numerical Methods for Electrical Discharge Modeling," AIAA Paper 2010-4632.

[66]Poggie, J., Adamovich, I., Bisek, N., and Nishihara, M., "Numerical simulation of nanosecond-pulse electrical discharges," *Plasma Sources Science and Technology*, Vol. 22, 2013, pp. 015001.

[67]Poggie, J., Bisek, N. J., Leger, T., and Tang, R., "Implicit Large-Eddy Simulation of a Supersonic Turbulent Boundary Layer: Code Comparison," AIAA Paper 2014-0423, 2014.

[68]Poggie, J., "Large-Scale Structures in Implicit Large-Eddy Simulation of Compressible Turbulent Flow," AIAA Paper 2014-3328, June 2014.

[69]White, F. M., *Viscous Fluid Flow*, McGraw-Hill, New York, 2nd ed., 1991.

[70]Visbal, M. R. and Gaitonde, D. V., "On the Use of Higher-Order Finite-Difference Schemes on Curvilinear and Deforming Meshes," *Journal of Computational Physics*, Vol. 181, 2002, pp. 155–185.

[71]Visbal, M. R. and Gaitonde, D. V., "Shock Capturing Using Compact-Differencing-Based Methods," AIAA Paper 2005-1265.

[72]Beam, R. and Warming, R., "An Implicit Factored Scheme for the Compressible Navier-Stokes Equations," *AIAA Journal*, Vol. 16, No. 4, 1978, pp. 393–402.

[73]Pulliam, T. H., "Implicit Finite-Difference Simulations of Three-Dimensional Compressible Flow," *AIAA Journal*, Vol. 18, No. 2, 1980, pp. 159–167.

[74]Hoffmann, K. A. and Chiang, S. T., *Computational Fluid Dynamics*, Engineering Educational System, Wichita KS, 4th ed., 2000.

[75]Thomas, P. D. and Lombard, C. K., "Geometric Conservation Law and Its Application to Flow Computations on Moving Grids," *AIAA Journal*, Vol. 17, No. 10, 1979, pp. 1030–1037.

[76]Pulliam, T. H. and Chaussee, D. S., "A Diagonal Form of an Implicit Approximate-Factorization Algorithm," *Journal of Computational Physics*, Vol. 39, 1981, pp. 347–363.

[77]Lele, S. K., "Compact Finite Difference Schemes with Spectral-Like Resolution," *Journal of Computational Physics*, Vol. 103, 1992, pp. 16–42.

[78]Gaitonde, D. V. and Visbal, M. R., "High-Order Schemes for Navier-Stokes Equations: Algorithm Implementation into FDL3DI," Technical Report AFRL-VA-WP-TR-1998-3060, Air Force Research Laboratory, Wright-Patterson Air Force Base, Ohio, August 1998.

[79]Chandra, R., Dagum, L., Kohr, D., Maydan, D., McDonald, J., and Menon, R., *Parallel Programming in OpenMP*, Academic Press, San Diego, 2001.

[80]Gropp, W., Lusk, E., and Skjellum, A., *Using MPI: Portable Parallel Programming with the Message-Passing Interface*, The MIT Press, Cambridge, MA, 2nd ed., 1999.

[81]Bisek, N. J., Rizzetta, D. P., and Poggie, J., "Plasma Control of a Turbulent Shock Boundary-Layer Interaction," *AIAA Journal*, Vol. 51, No. 8, 2013, pp. 1789–1804.

[82]Mullenix, N. J., Gaitonde, D. V., and Visbal, M. R., "Spatially Developing Supersonic Turbulent Boundary Layer with a Body-Force Based Method," *AIAA Journal*, Vol. 51, No. 8, 2013, pp. 1805–1819.

[83]Bendat, J. S. and Piersol, A. G., *Random Data: Analysis and Measurement Procedures*, J. Wiley, New York, 2nd ed., 1986.

[84]Pope, S. B., *Turbulent Flows*, Cambridge University Press, Cambridge, UK, 2000.

[85]Smith, D. R., Poggie, J., Konrad, W., and Smits, A. J., "Visualization of the Structure of Shock Wave Turbulent Boundary Layer Interactions using Rayleigh Scattering," AIAA Paper 91-0651.

[86]Reichardt, H., "Vollständige Darstellung der turbulenten Geschwindigkeitsverteilung in glatten Leitungen," *Zeitschrift für Angewandte Mathematik und Mechanik*, Vol. 31, No. 7, 1951, pp. 208–219.

[87]Éléna, M. and Lacharme, J. P., "Experimental Study of a Supersonic Turbulent Boundary Layer Using a Laser Doppler Anemometer," *Journal Mécanique Théorique et Appliquée*, Vol. 7, 1988, pp. 175–190.

[88]Alving, A. E., *Boundary Layer Relaxation from Convex Curvature*, Ph.D. dissertation, Princeton University, Princeton NJ, 1988.

[89]Konrad, W., *A Three-Dimensional Supersonic Turbulent Boundary Layer Generated by an Isentropic Compression*, Ph.D. Dissertation, Princeton University, Princeton NJ, 1993.

[90]Poggie, J., *Quantitative Flow Visualization Applied to the Study of Compressible Turbulent Flow*, Master's thesis, Princeton University, June 1991.

[91]Selig, M. S., Andreopoulos, J., Muck, K. C., Dussauge, J. P., and Smits, A. J., "Turbulence Structure in a Shock Wave / Turbulent Boundary-Layer Interaction," *AIAA Journal*, Vol. 27, No. 7, 1989, pp. 862–869.

[92]Sreenivasan, K. R., Ramshankar, R., and Meneveau, C., "Mixing, Entrainment and Fractal Dimensions of Surfaces in Turbulent Flows," *Proceedings of the Royal Society of London A*, Vol. 421, No. 1860, 1989, pp. 79–108.

[93]Saddoughi, S. G. and Veeravalli, S. V., "Local Isotropy in Turbulent Boundary Layers at High Reynolds Number," *Journal of Fluid Mechanics*, Vol. 268, 1994, pp. 333–372.

[94]Poggie, J., Bisek, N. J., Kimmel, R. L., and Stanfield, S. A., "Spectral Characteristics of Separation Shock Unsteadiness," *AIAA Journal*, 2014, Accepted for publication. DOI: 10.2514/1.J053029.

[95]Jones, W. P. and Launder, B. E., "The Prediction of Laminarization with a two-equation model of turbulence," *International Journal of Heat and Mass Transfer*, Vol. 15, No. 2, 1972, pp. 301–314.

[96]Clauser, F. H., "The Turbulent Boundary Layer," *Advances in Applied Mechanics*, Vol. 4, 1956, pp. 1–51.

[97]Klebanoff, P., "Characteristics of turbulence in a boundary layer with zero pressure gradient." Technical Report NACA-TR-1247, National Advisory Council for Aeronautics, January 1955.

Reference	M_∞	$\mathrm{Re}_{\theta i}$	δ^+	T_w/T_{aw}	L_3/δ	Δx_1^+	$(\Delta x_2^+)_w$	$(\Delta x_2^+)_e$	Δx_3^+
Coleman et al.[25,26]	1.5–3.0					17–39	0.1–0.2		10–24
Rai et al.[27]	2.3			1.0	3.8	27	0.95		10
Guarini et al.[28]	2.5	850		1.0		8.9	0.48	7.8	5.9
Urbin and Knight[30]	3.0			1.0	0.87–3.5	11–56	0.9–1.7		3.1–26
Maeder et al.[29]	3.0–6.0	500–1200		0.95–0.96	0.84–1.4	1.3–2.9	~ 0.4		1.2–2.2
Stolz and Adams[31]	2.5	2200–4900		1.1		41–59	2.7–3.6		21–29
Pirozzoli et al.[32]	2.3	2300		1.0	2.1	15	1.1		6.6
Rizzetta and Visbal[33]	2.3	1900		1.0	3.8	84	0.9		22
Sagaut et al.[34]	2.3				1.4	50	1.0		18
Xu and Martin[35]	4.0				1.4	13	0.12	570	4.8
Martin[36]	3.0–6.0		330–400	1.0	1.7–2.3	7.2–8.0	~ 0.3		2.7–3.0
Pirozzoli et al.[37]	2.0	860	360	1.0	2.9	4.5	0.95	4.1	4.5
Ringuette et al.[38]	2.9–3.0		330–480		2.2–2.3	8.0–9.3			3.0–5.8
Duan et al.[39]	5.0	1500	390–800	0.18–1.0	1.8–2.6	7.4–7.8	0.30–0.33		2.8–3.0
Duan et al.[41]	0.3–12	1500–1600	380-570		2.4–2.9	6.8–8.4	0.10–0.30		2.3–3.1
Lagha et al.[43]	2.5–20		300–340	1.0	2	8	0.30	11	3
Lagha et al.[43]	5.0		380	0.47–5.4					
Pirozzoli et al.[44,46]	2.0	720–16000	250–4000	1.0		5.2–6.5	0.7–0.9	6.5–17	4.5–5.9

Table 1. Resolution and conditions reported in the literature for ILES and DNS of supersonic turbulent boundary layers.

Parameter	Value
δ_0	0.610 mm
U_∞	588 m/s
p_∞	23.8 kPa
T_∞	170 K
T_w	323 K
M	2.25
$U_\infty \delta_0 / \nu_\infty$	1.5×10^4

Table 2. Flow conditions for Mach 2.3 turbulent boundary layer.

Parameter	Value
δ_0	4.00 mm
U_∞	795 m/s
p_∞	4.98 kPa
T_∞	65.5 K
T_w	321 K
M	4.9
$U_\infty \delta_0 / \nu_\infty$	1.9×10^5

Table 3. Flow conditions for Mach 4.9 turbulent boundary layer.

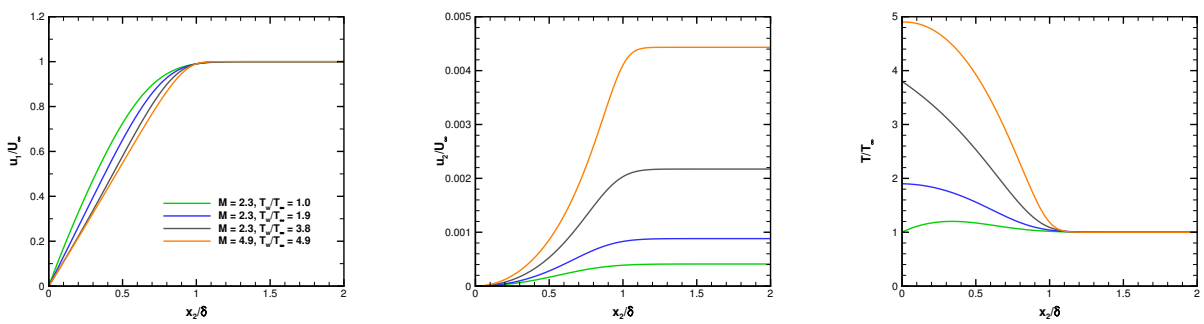

(a) Streamwise velocity. (b) Wall-normal velocity. (c) Temperature.

Figure 1. Laminar boundary layer profiles used for inflow boundary conditions. Flow conditions correspond to Tables 2–3, with varying wall temperature.

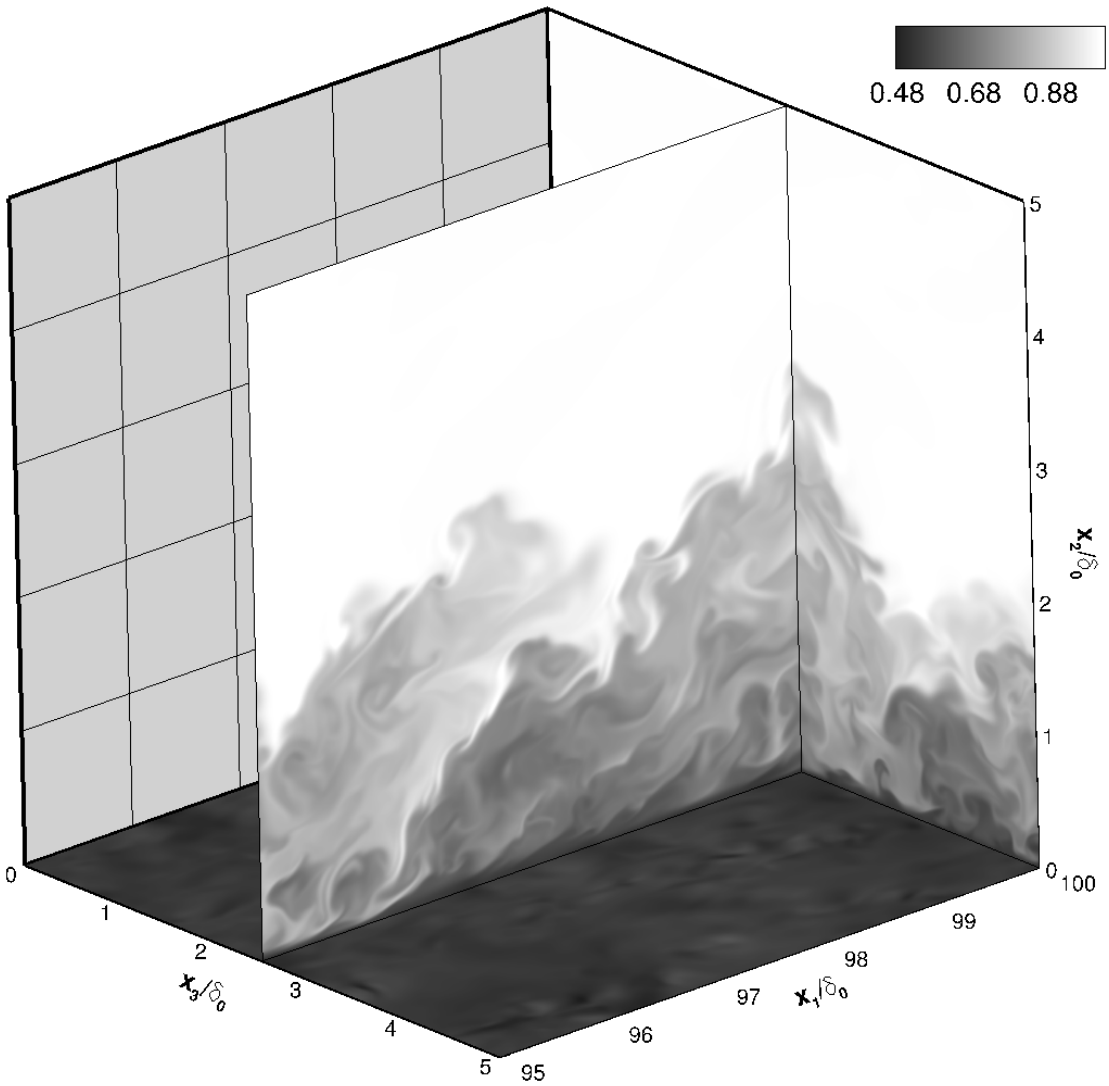

Figure 2. Sample density field ρ/ρ_∞ for the turbulent boundary layer at $M = 2.3$ on Grid 5 ($\Delta x_1^+ = 1$, $\Delta x_2^+ = 0.9$, $\Delta x_3^+ = 1$.). The field of view is a cube with side of about 2δ. Local conditions at $x_1/\delta_0 = 100$: $\mathrm{Re}_{\theta i} = 2000$, $C_f = 2.3 \times 10^{-3}$, $\delta^+ = 570$.

Grid	N_1	N_2	N_3	N	L_1/δ_0	L_2/δ_0	L_3/δ_0
1	526	151	130	1.0×10^7	100	5	5
2	2278	1277	117	3.4×10^8	100	5	5
3	4026	276	255	2.8×10^8	100	5	5
3W	4026	276	505	5.6×10^8	100	10	5
3VW	4026	276	1005	1.1×10^9	100	20	5
4	11287	1277	568	8.2×10^9	100	5	5
5	22548	1277	1131	3.3×10^{10}	100	5	5

Table 4. Properties of the computational meshes for $M = 2.3$, $T_w = T_{aw}$ cases.

Grid	M_∞	$\mathrm{Re}_{\theta i}$	δ^+	T_w/T_{aw}	L_3/δ	Δx_1^+	$(\Delta x_2^+)_w$	$(\Delta x_2^+)_e$	Δx_3^+
1	2.3	1900	640	1.0	2.0	45	0.9	19	9
2	2.3	2000	560	1.0	2.0	10	0.9	0.9	10
3	2.3	2000	560	1.0	2.0	6	0.5	9	5
3W	2.3	2000	560	1.0	4.0	6	0.5	9	5
3VW	2.3	2000	570	1.0	8.0	6	0.5	9	5
4	2.3	2000	570	1.0	2.0	2	0.9	0.9	2
5	2.3	2000	570	1.0	2.0	1	0.9	0.9	1

Table 5. Resolution and conditions for present simulations with $M = 2.3$, $T_w = T_{aw}$, nondimensionalized using conditions at the reference station $x_1/\delta_0 = 100$.

M	T_w/T_{aw}	$\mathrm{Re}_{\theta i}$	δ^+	L_3/δ	Δx_1^+	$(\Delta x_2^+)_w$	Δx_3^+
2.3	0.52	3500	1200	2.2	14	0.5	11
2.3	1.0	2000	560	2.0	6	0.5	5
2.3	2.0	1000	250	2.0	2	0.2	2
4.9	0.93	4000	750	2.8	11	0.4	9

Table 6. Properties of the computational mesh for different cases, nondimensionalized using conditions at the reference station $x_1/\delta_0 = 100$. For each case the size of the mesh was $4026 \times 276 \times 255$ for a total of 2.8×10^8 points.

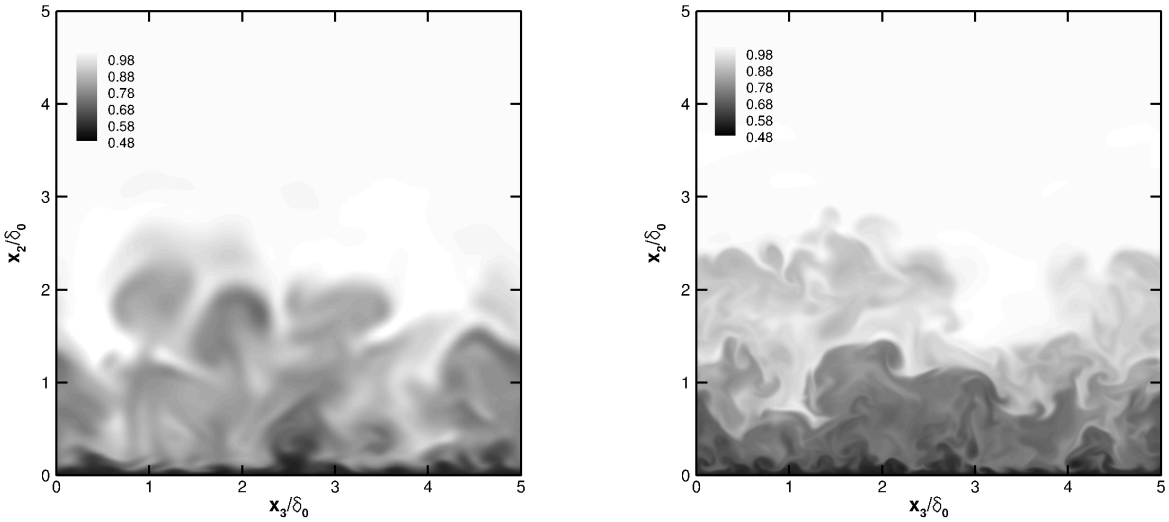

(a) Grid 1: $\Delta x_1^+ = 45$, $\Delta x_2^+ = 0.9 - 19$, $\Delta x_3^+ = 9$.

(b) Grid 5: $\Delta x_1^+ = 1$, $\Delta x_2^+ = 0.9$, $\Delta x_3^+ = 1$.

Figure 3. Sample density fields (ρ/ρ_∞) in the $x_1/\delta_0 = 100$ plane for the turbulent boundary layer at $M = 2.3$.

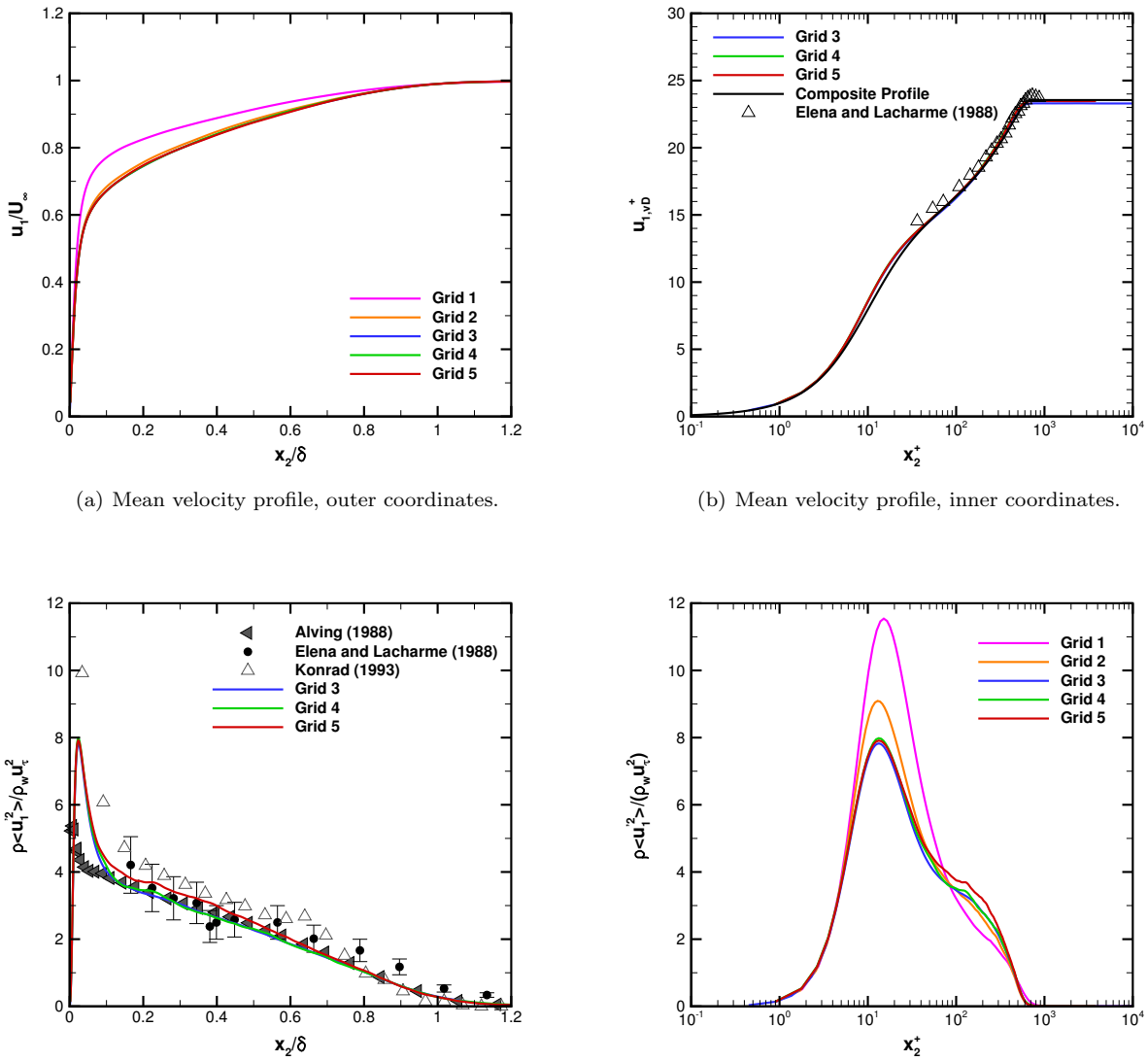

(a) Mean velocity profile, outer coordinates.

(b) Mean velocity profile, inner coordinates.

(c) Reynolds normal stress, outer coordinates.

(d) Reynolds normal stress profile, inner coordinates.

Figure 4. Effect of spatial resolution on boundary layer profiles.

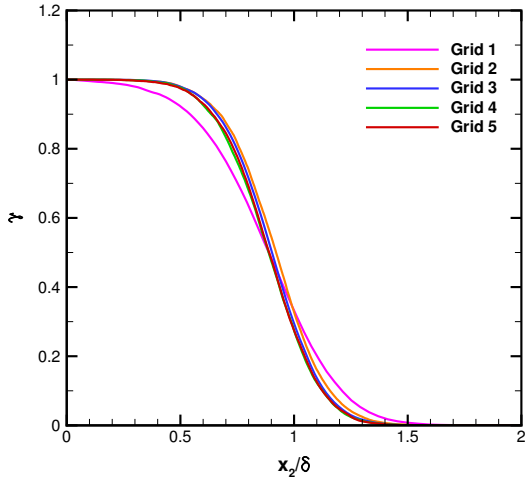

(a) Intermittency profiles through the boundary layer (threshold $0.975\rho_\infty$).

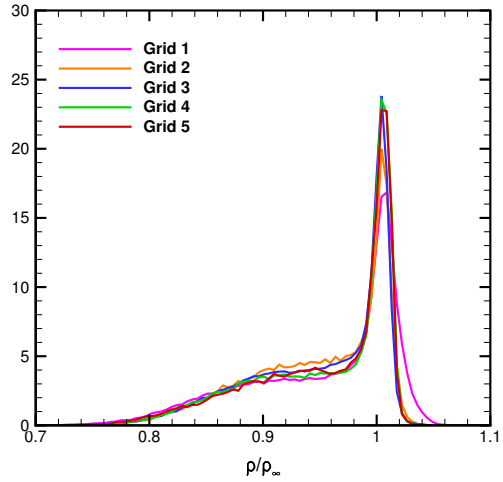

(b) Probability density function of density at $y/\delta = 0.9$.

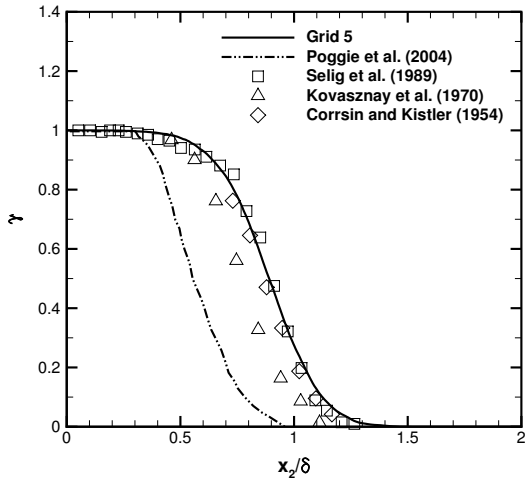

(c) Computed intermittency profile compared to hotwire measurements[7,11,91] and condensate-enhanced Rayleigh scattering data.[19]

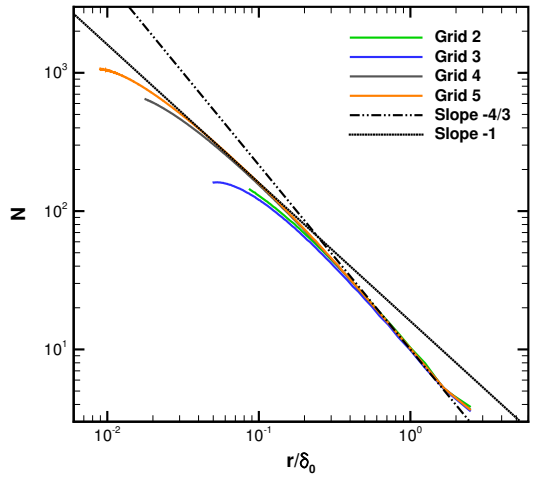

(d) Boxcounting algorithm applied to $0.975\rho_\infty$ contour.

Figure 5. Effect of spatial resolution on intermittency of the density field.

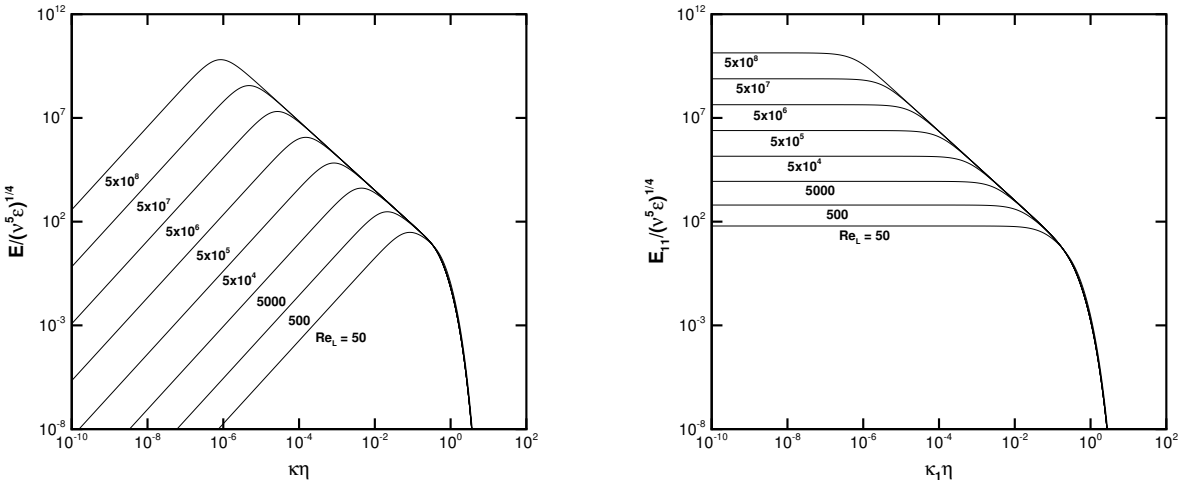

(a) Three-dimensional spectrum.

(b) Longitudinal one-dimensional spectrum.

Figure 6. Pope's model spectrum[84] for isotropic turbulence.

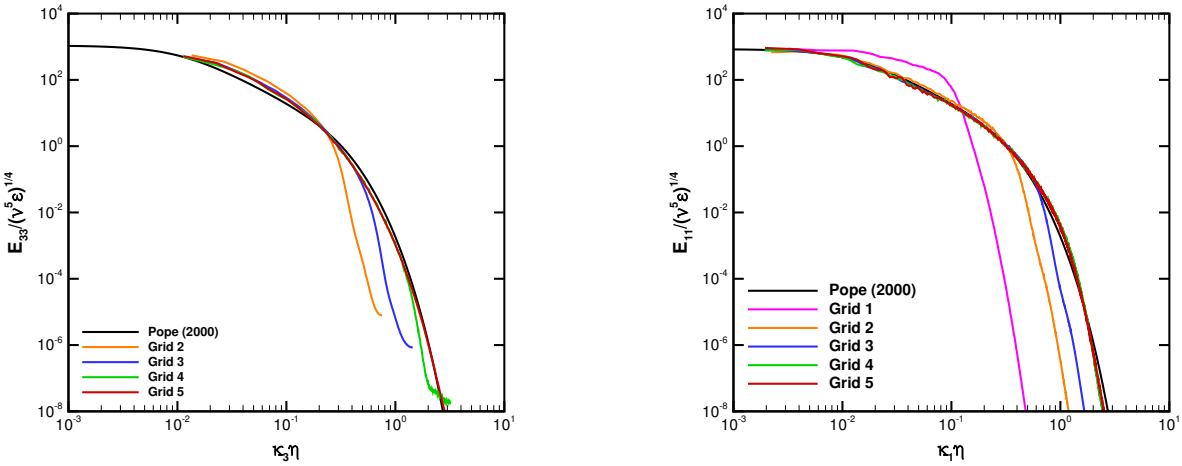

(a) Longitudinal spectrum $E_{33}(\kappa_3)$.

(b) Longitudinal spectrum $E_{11}(\kappa_1)$.

Figure 7. Effect of spatial resolution on spectra at $x_1/\delta_0 = 100$, $x_2/\delta = 0.5$ for the turbulent boundary layer at $M = 2.3$. The wavenumber corresponding to the Kolmogorov length scale is $\kappa_i\eta = 2\pi \approx 6$.

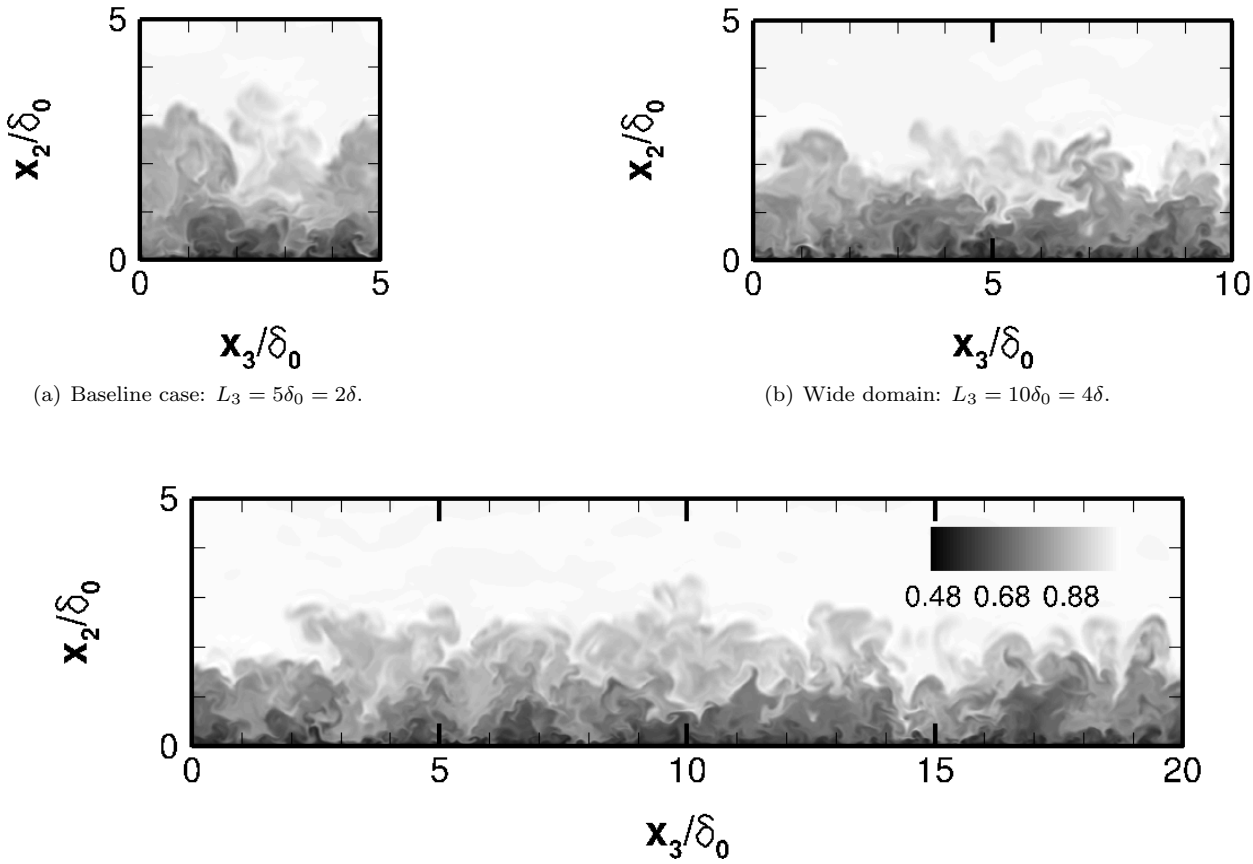

(a) Baseline case: $L_3 = 5\delta_0 = 2\delta$.

(b) Wide domain: $L_3 = 10\delta_0 = 4\delta$.

(c) Very wide domain: $L_3 = 20\delta_0 = 8\delta$.

Figure 8. Effect of domain width: sample density fields (ρ/ρ_∞) in the $x_1/\delta_0 = 100$ plane for the turbulent boundary layer at $M = 2.3$.

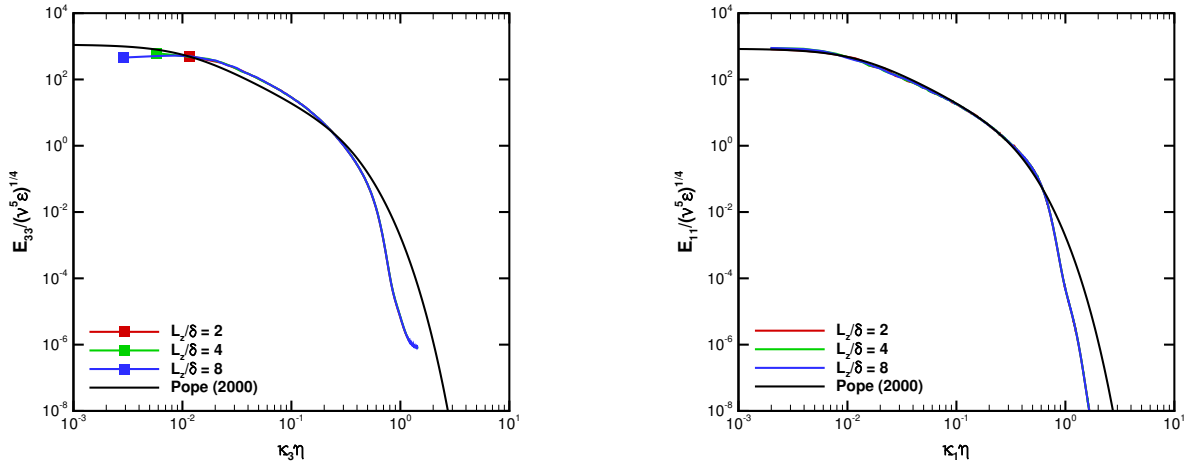

(a) Longitudinal wavenumber spectrum $E_{33}(\kappa_3)$.

(b) Longitudinal temporal spectrum $E_{11}(\kappa_1)$.

Figure 9. Effect of domain width on velocity spectra at $x_1/\delta_0 = 100$, $x_2/\delta = 0.5$ for the turbulent boundary layer at $M = 2.3$. The wavenumber corresponding to the Kolmogorov length scale is $\kappa_i\eta = 2\pi \approx 6$.

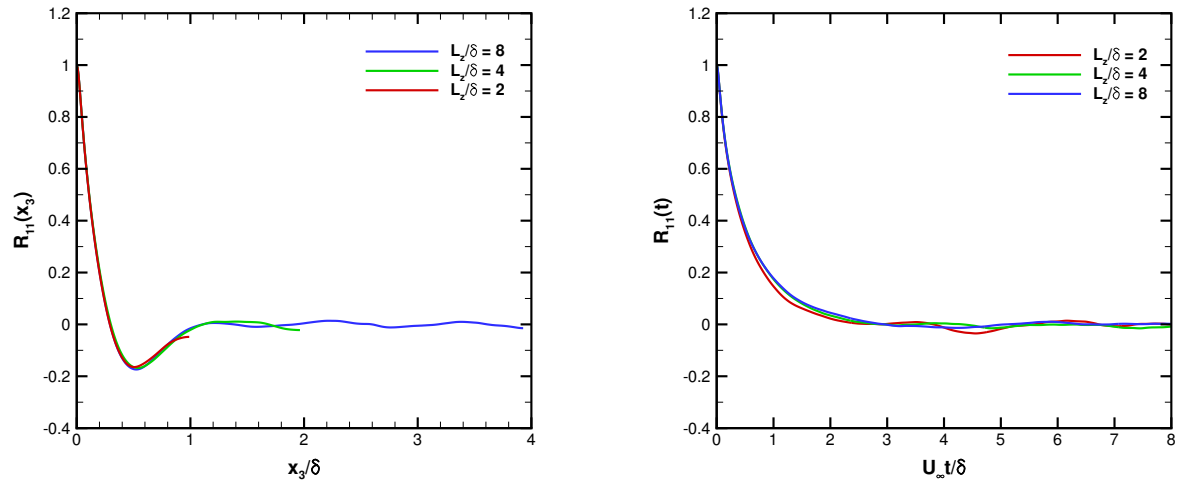

(a) Transverse spatial correlation $R_{11}(x_3)$.

(b) Temporal correlation $R_{11}(t)$.

Figure 10. Effect of domain width on velocity correlations at $x_1/\delta_0 = 100$, $x_2/\delta = 0.5$ for the turbulent boundary layer at $M = 2.3$.

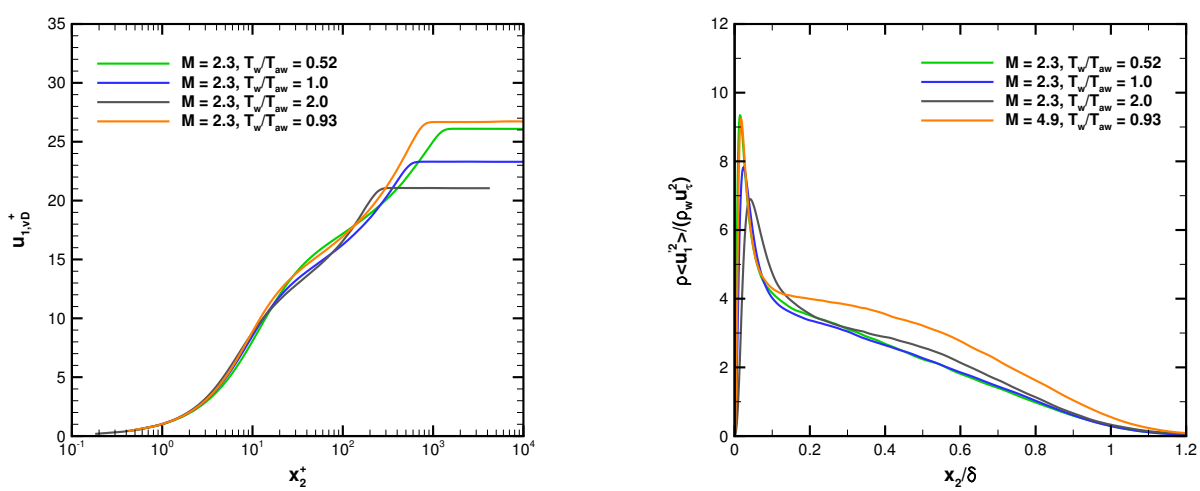

(a) Mean velocity profiles in van Driest transformed inner coordinates.

(b) Reynolds normal stress profiles in outer coordinates.

Figure 11. Test of van Driest[22] and Morkovin[21] scaling.

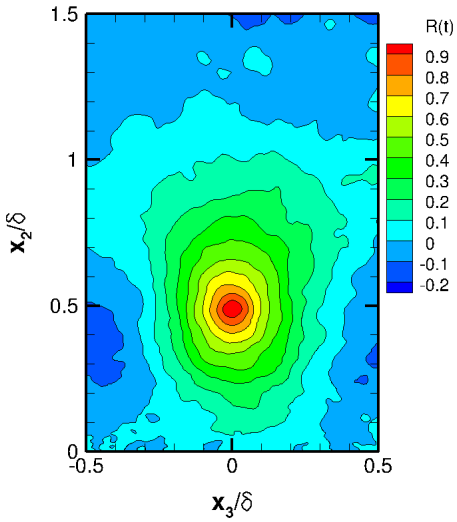

(a) Streamwise mass flux correlations in end plane $x_1/\delta_0 = 90$. $M = 2.3$, $T_w/T_{aw} = 1.0$, $\delta^+ = 560$. Reference point: $(90\delta_0, 0.5\delta, 2.5\delta_0)$.

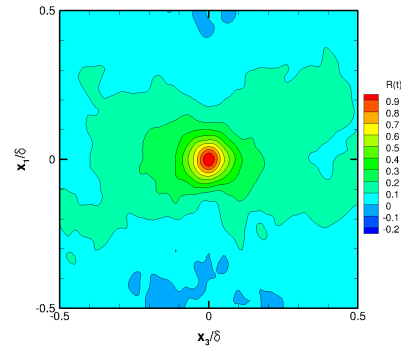

(b) Wall pressure correlations. $M = 2.3$, $T_w/T_{aw} = 1.0$, $\delta^+ = 560$. Reference point: $(90\delta_0, 0, 2.5\delta_0)$.

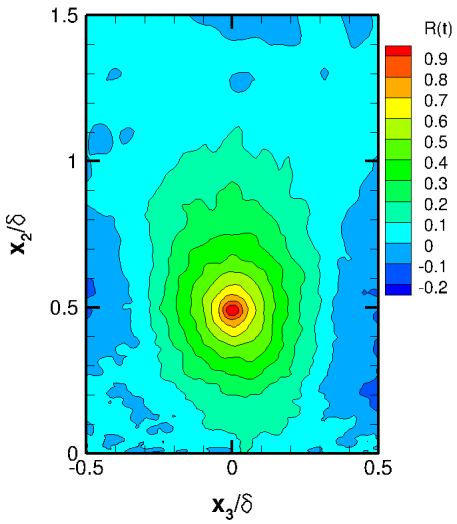

(c) Streamwise mass flux correlations in end plane $x_1/\delta_0 = 90$. $M = 4.9$, $T_w/T_{aw} = 0.93$, $\delta^+ = 730$. Reference point: $(90\delta_0, 0.5\delta, 2.5\delta_0)$.

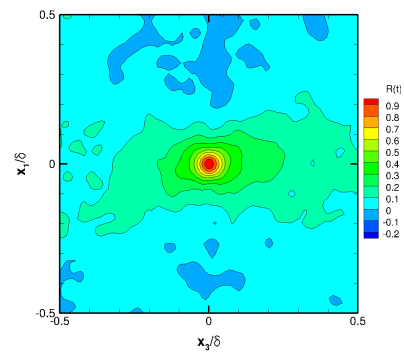

(d) Wall pressure correlations. $M = 4.9$, $T_w/T_{aw} = 0.93$, $\delta^+ = 730$. Reference point: $(90\delta_0, 0, 2.5\delta_0)$.

Figure 12. Spatial correlations: Mach number effect.

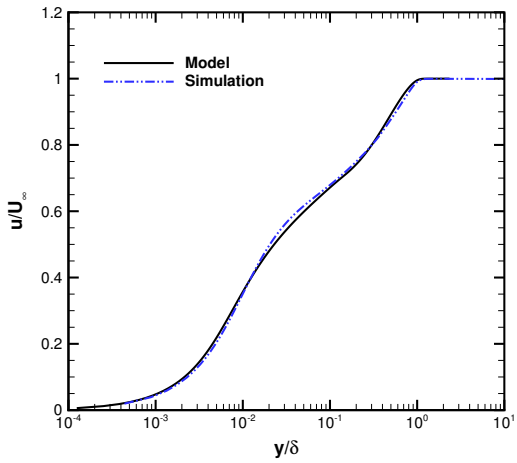

(a) $M = 2.3$, $T_w/T_{aw} = 0.52$, $\delta^+ = 1200$.

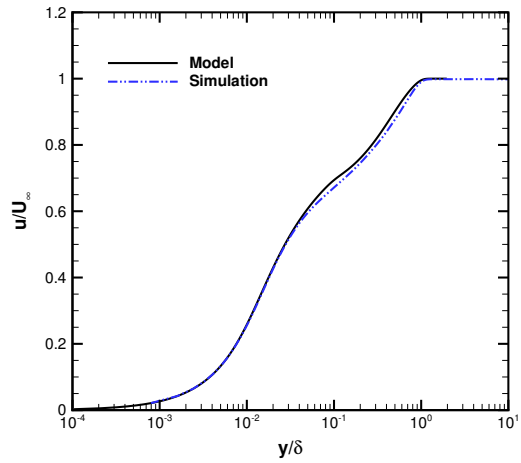

(b) $M = 2.3$, $T_w/T_{aw} = 1.0$, $\delta^+ = 560$.

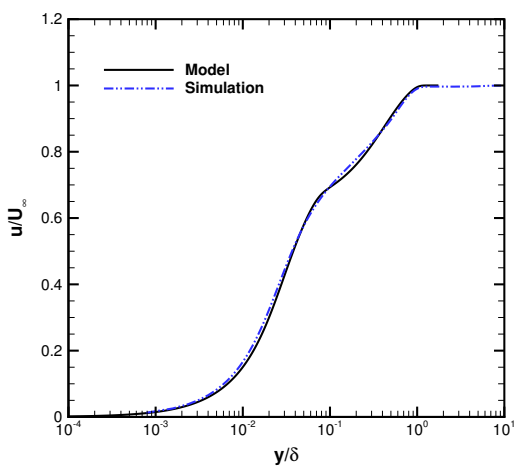

(c) $M = 2.3$, $T_w/T_{aw} = 2.0$, $\delta^+ = 250$.

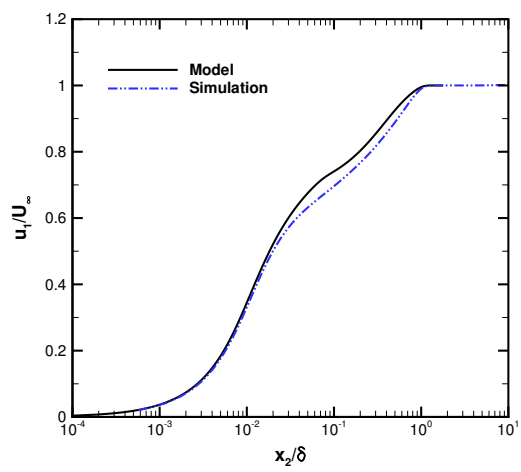

(d) $M = 4.9$, $T_w/T_{aw} = 0.93$, $\delta^+ = 730$.

Figure 13. Profiles of mean streamwise velocity.

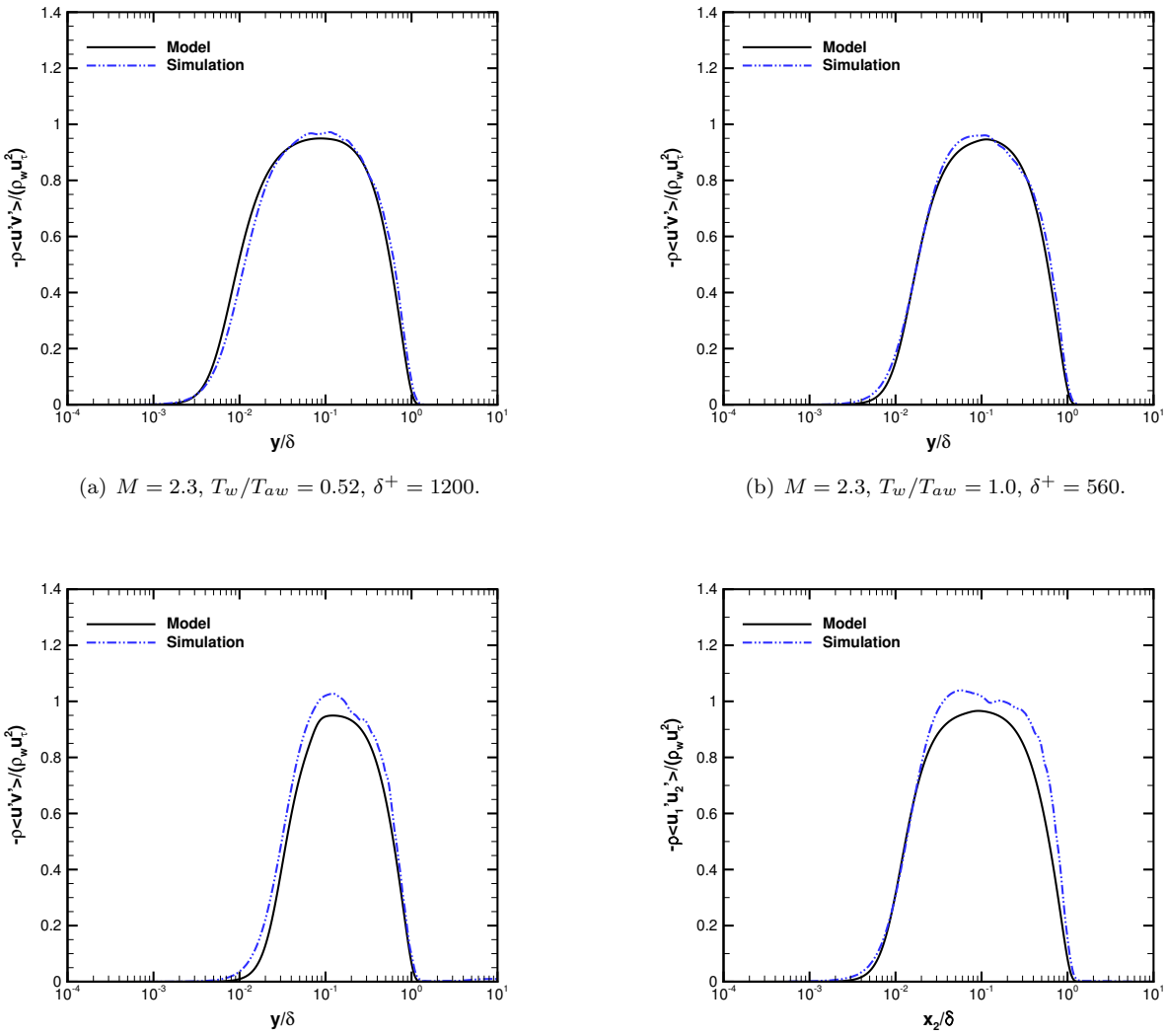

(a) $M = 2.3$, $T_w/T_{aw} = 0.52$, $\delta^+ = 1200$.

(b) $M = 2.3$, $T_w/T_{aw} = 1.0$, $\delta^+ = 560$.

(c) $M = 2.3$, $T_w/T_{aw} = 2.0$, $\delta^+ = 250$.

(d) $M = 4.9$, $T_w/T_{aw} = 0.93$, $\delta^+ = 730$.

Figure 14. Profiles of Reynolds shear stress.

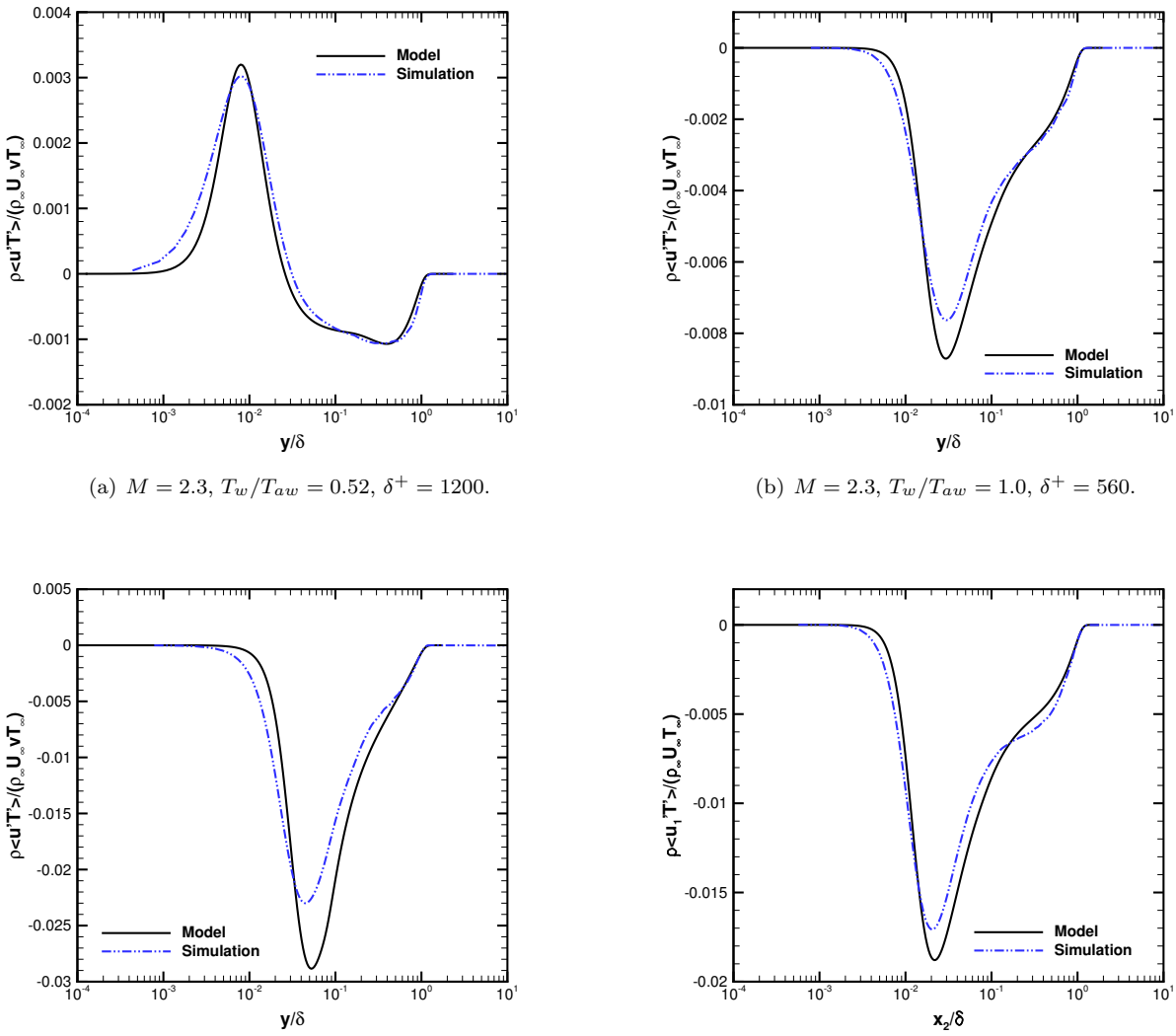

(a) $M = 2.3$, $T_w/T_{aw} = 0.52$, $\delta^+ = 1200$.

(b) $M = 2.3$, $T_w/T_{aw} = 1.0$, $\delta^+ = 560$.

(c) $M = 2.3$, $T_w/T_{aw} = 2.0$, $\delta^+ = 250$.

(d) $M = 4.9$, $T_w/T_{aw} = 0.93$, $\delta^+ = 730$.

Figure 15. Streamwise turbulent energy flux.

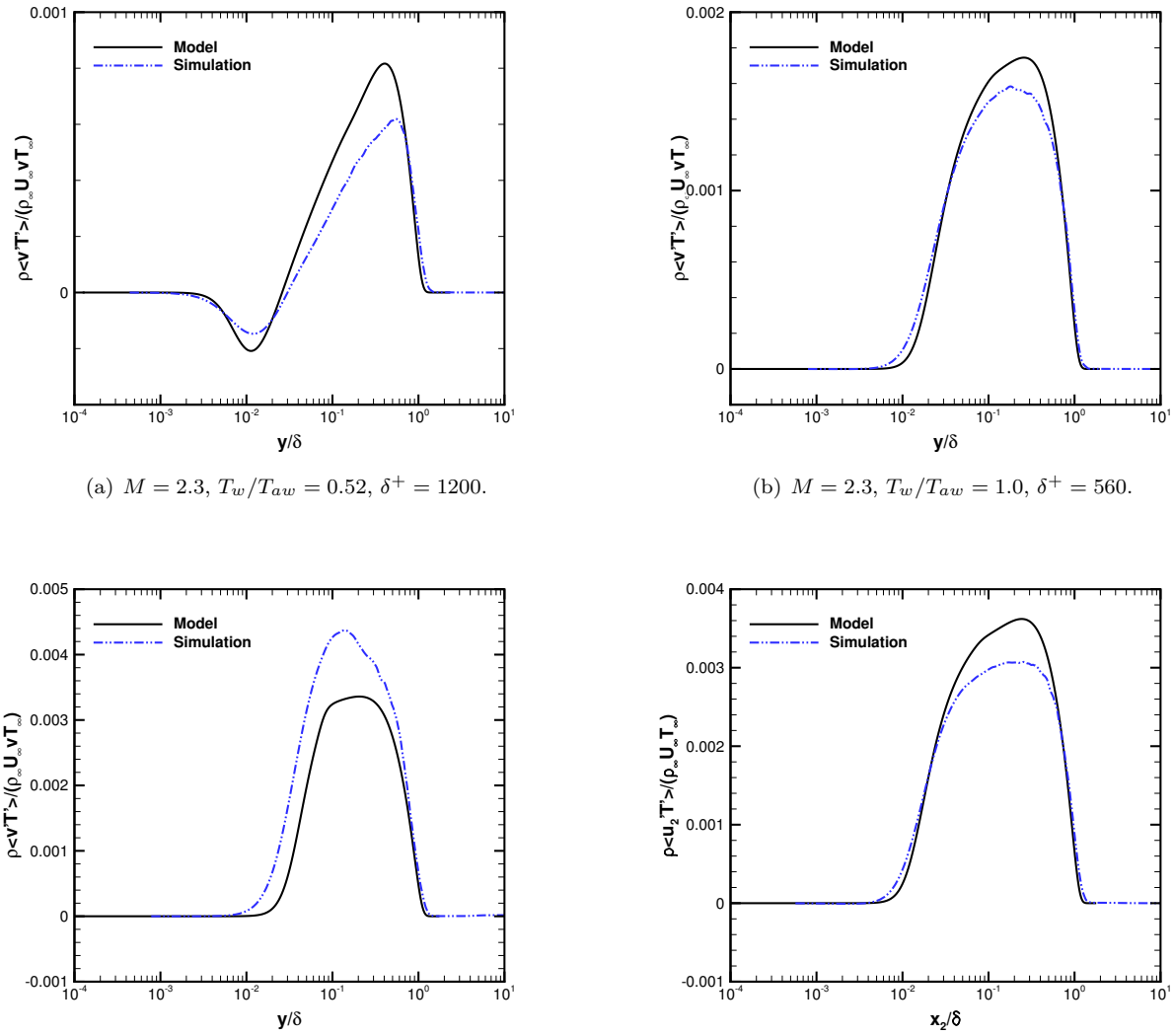

(a) $M = 2.3$, $T_w/T_{aw} = 0.52$, $\delta^+ = 1200$.

(b) $M = 2.3$, $T_w/T_{aw} = 1.0$, $\delta^+ = 560$.

(c) $M = 2.3$, $T_w/T_{aw} = 2.0$, $\delta^+ = 250$.

(d) $M = 4.9$, $T_w/T_{aw} = 0.93$, $\delta^+ = 730$.

Figure 16. Transverse turbulent energy flux.

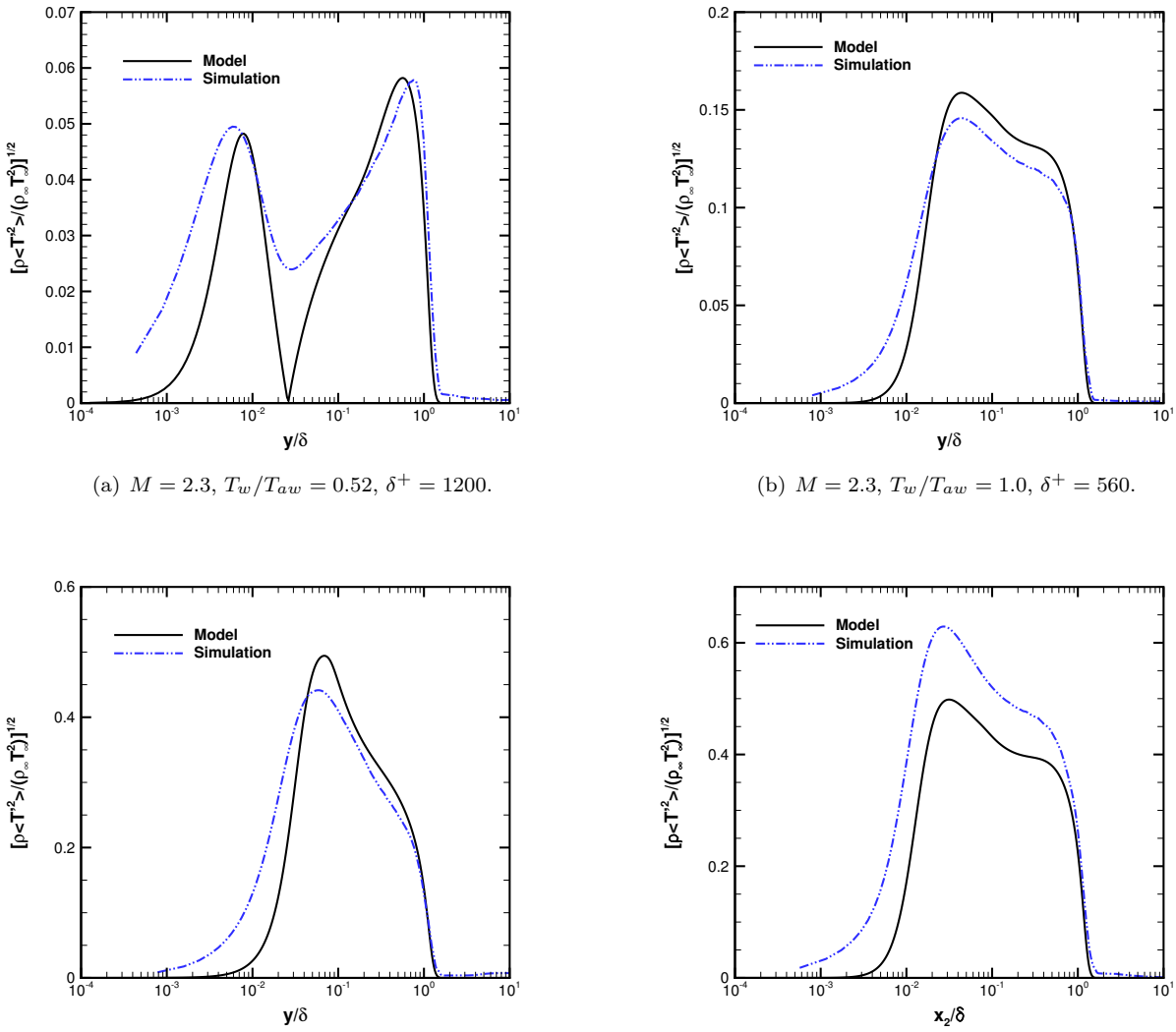

(a) $M = 2.3$, $T_w/T_{aw} = 0.52$, $\delta^+ = 1200$.

(b) $M = 2.3$, $T_w/T_{aw} = 1.0$, $\delta^+ = 560$.

(c) $M = 2.3$, $T_w/T_{aw} = 2.0$, $\delta^+ = 250$.

(d) $M = 4.9$, $T_w/T_{aw} = 0.93$, $\delta^+ = 730$.

Figure 17. Temperature fluctuations.